Nanoscale Advances

ROYAL SOCIETY OF CHEMISTRY

PAPER

View Article Online
View Journal

Cite this: DOI: 10.1039/d5na00948k

A glyco-engineered nanoplatform for fluorescence detection and adsorptive elimination of *E. coli* from water

Archana P. K., Vidhya C. Valsalakumar, Suni Vasudevan and Unnikrishnan Gopalakrishna Panicker *

Rapid and sensitive detection and removal of *Escherichia coli* (*E. coli*) in environmental and clinical settings are crucial to prevent infections and to ensure water safety. In this study, we introduce a multifunctional mannosylated graphene oxide (MAN-GO) composite that enables both fluorescence detection and adsorption of *E. coli*, leveraging the specific interactions between mannose and *E. coli* fimbriae. The MAN-GO composite demonstrated a limit of detection (LOD) as low as 1.382×10^4 CFU mL^{-1} in fluorimetric assays, showcasing high sensitivity and selectivity, even in the presence of interfering species. Adsorption studies reveal that MAN-GO exhibits a maximum adsorption capacity of 448.219 CFU g^{-1}, with a rapid equilibrium time of 120 minutes, following a pseudo-second-order kinetic model and fitting well with the Langmuir adsorption isotherm (in this work, CFU g^{-1} is defined based on the wet mass of the sample for consistency). The maximum adsorption efficiency of the system was identified to be 88.21%, reflecting a highly effective interaction between the adsorbent and the target analyte. The results underscore the potential of the developed material for efficient adsorption applications and indicate its viability for further optimization in practical scenarios. The highly effective adsorption process, driven by the affinity of mannose-functionalized graphene oxide, facilitates a "green" capture and removal of *E. coli* from aqueous solutions without the need for additional chemical agents. Together, the fluorescent sensing capability and adsorption performance of MAN-GO highlight its potential as a dual-functional material for both the monitoring and mitigation of microbial contamination in aqueous systems, offering a sustainable approach to microbial detection and remediation.

Received 7th October 2025
Accepted 6th March 2026

DOI: 10.1039/d5na00948k

rsc.li/nanoscale-advances

1 Introduction

Nanomaterial-based sensors have greased the wheels in the development of tremendously potent devices as feasible systems in the fields of food,[1] water,[2] healthcare,[3] medicine,[4] energy,[5] electronics,[6] defence,[7] consumer products,[8] environment,[9] and many other fields. While nanotechnology is influential across diverse disciplines, its most pivotal contributions lie in the medical and healthcare sectors, making it a highly sought-after research theme. Despite numerous advancements, several constraints remain to be addressed to develop health-monitoring nanosystems that are compact, long-term, multifunctional, real-time, pervasive, and affordable.[10] These challenges encompass biocompatibility, reliability, stability, comfort, convenience, miniaturization, cost, and biofouling. Even in the 21st century, overcoming these hurdles continues to be a formidable challenge.[11] Nanobiosensors, which generally assess the levels of biological markers or any chemical reaction by generating distinct signals that are primarily associated with the concentration of an analyte, have the potential to boost diagnostic precision and treatment efficacy.[12] Biosensors based on nanocomposites have garnered much acceptance in the past few years as they offer versatile applications for sensing in environmental, medical, and diagnostic studies.[13–16] The progress in technology has led to the integration of nanobiosensors with all scientific fields, particularly for the detection of pathogenic bacteria and viruses in water, air, blood, serum, and beyond.[17] Nanocomposite-based biosensors are now vital for various routine analyses of clinical samples and for monitoring a spectrum of environmental toxins and pathogens. Cost-effective, highly sensitive, and selective sensors can be made from nanocomposites, which are specifically capable of detecting abundant bacteria like *E. coli*, surpassing traditional detection methods.[18]

Escherichia coli is detected in every mammal's excrement at a concentration greater than 10^4 CFU g^{-1}, which may vary from animal to animal.[19] While both other bacteria and viruses are susceptible to oxidation, *E. coli* persists in drinking water for 4 to 12 weeks based on the surrounding conditions. Voltammetric and amperometric methods, polymerase chain reaction (PCR) tests, enzyme and non-enzyme linked immunoassays, and

Department of Chemistry, National Institute of Technology Calicut, Calicut, Kerala 673601, India. E-mail: unnig@nitc.ac.in

optical techniques such as spectroscopy and fluoroscopy are being used for the identification of bacteria; however, commonly used techniques are biochemical tests like culturing techniques and pour plate methods.[20] The efficacy of these methods, however, relies on distinct performance standards that can vary depending on parameters such as concentration of bacteria, chemical agents used, antigen–antibody binding, sample volume used and response time.[21] A 2D nanomaterial sensor platform is a prime option for the rapid and accurate detection and identification of disease causing microorganisms.[22,23]

Graphene oxide (GO), the oxidized form of graphene laced with oxygen containing groups, is a promising material for the early diagnosis of diseases, which possesses and plays a vital role in the healthcare sector.[24] GO-based biosensors are capable of detecting and monitoring relevant biomarkers, offering opportunities for a better understanding of various physiological and pathological processes.[25] Owing to their versatility, biocompatibility, small size, large surface area, and potential to interact with different biological cells and tissues, GO-based biosensors have generated tremendous interest by now, resulting in significant advances and promising application prospects.[11,26,27] Moreover, GO based hybrid nanomaterials have demonstrated significant potential in wastewater treatment, effectively removing organic pollutants and inhibiting microbial growth, thus contributing to improved water quality and environmental sustainability.[28–30] Herein, we present a binary glyco-functionalized graphene oxide-based composite specially designed for *E. coli* sensing and adsorption. The system has been developed using D-mannose, the sugar monomer of the aldohexose series of carbohydrates, and the C-2 epimer of glucose. The synergistic effect of specific mannose recognition and the interaction of bacteria with graphene oxide layers transforms the system into an ideal material for the sensing and adsorption of bacteria. To the best of our knowledge, this is the first report on combining mannose functionalization with graphene oxide in a composite system, thereby achieving both selective sensing and efficient bacterial adsorption. Importantly, the system demonstrates an excellent limit of detection along with high adsorption efficiency, highlighting its strong potential for biomedical and environmental applications.

2 Experimental section

2.1 Materials

Graphite (Sigma-Aldrich, 99.99%), aniline (Sigma-Aldrich, ≥99.5%), sulfuric acid (Merck, 98%), hydrochloric acid (Merck, 37%), sodium nitrate (Merck, ≥99%), potassium permanganate (Sigma-Aldrich, ≥99%), 1-ethyl-3-(3-dimethylaminopropyl)carbodiimide (EDC, Thermo Fisher Scientific, ≥98%), *N*-hydroxysuccinimide (NHS, Thermo Fisher Scientific, ≥98%), D-mannose (Alfa Aesar, ≥99%), ethylenediamine (Merck, ≥99%), and dimethylformamide (DMF, Qualigens, ≥99%) were used as received without any further purification. Phosphate-buffered saline (PBS) was procured from Himedia Labs. All chemicals were of analytical grade. Double-distilled water was used throughout the experiments, including solution preparation, to ensure high purity and consistency.

Fourier transform infrared (FT-IR) spectra were recorded using a JASCO 4700 spectrophotometer in the 4000–500 cm^{-1} region. UV-visible absorption studies were carried out on a Shimadzu 2600 UV-visible spectrophotometer as well as on a Lambda 35 (PerkinElmer) spectrophotometer at a 480 nm min^{-1} scan rate. The particle size, distribution, and morphology of the samples were analysed using a field emission scanning electron microscope (FESEM, FEI QUANTA FEG 200) equipped with an energy dispersive X-ray spectrometer (EDS), operating at 30 kV with a take-off angle of 35° relative to the sample surface. Brunauer–Emmett–Teller (BET) analysis was carried out using BELSORP high-precision gas/vapor adsorption apparatus (BELMaster™ version 2.3.4). Raman spectral measurements were carried out using a LABRAM HR Evolution CCD model 1024X256-DE Raman microscope with an excitation wavelength of 532 nm from an Nd:YAG laser source with an acquisition time of 10 s. The chemical composition and nature of chemical bonding in the sample were further confirmed using the analysis of X-ray photoelectron spectroscopy (XPS), obtained using a Mg K_α source with an excitation energy of 1253.6 eV (Omicron Nanotechnology Ltd).

2.2 Methods

2.2.1 Synthesis of graphene oxide (GO). Graphene oxide was synthesized by a modified Hummer's method using powdered graphite flakes and $KMnO_4$.[31,32] A comprehensive outline of the synthesis procedure is given in Fig. 1.

2.2.2 Synthesis of mannosylated graphene oxide (MAN-GO). D-Mannose functionalization on GO was carried out through covalent functionalization following a previously reported procedure[33,34] (Fig. 2). Initially mannosylated ethylenediamine was synthesized from D-mannose and iodine (10 : 1) in methanol using sonochemical dissolution. Ethylenediamine was then added at a ratio of 1 : 6 (v/v) to methanol and the mixture was ultrasonicated for 1 hour, resulting in the formation of a white precipitate, mannosylated ethylenediamine (MAN-En), and the reaction mixture was kept overnight to ensure completion of the reaction. The precipitate formed was washed with ethanol and methanol to remove excess iodine, other impurities and byproducts. The product was dried in a hot air oven and stored at 4 °C for further reaction.

For the covalent coupling of MAN-En with GO, GO dispersion (1 mg mL^{-1} in DMF) was allowed to react with 1-ethyl-3-(3-dimethylaminopropyl)carbodiimide (EDC), *N*-hydroxysuccinimide (NHS) and MAN-En at a ratio of 4 : 4 : 6 relative to GO respectively, for 24 hours at room temperature. The product obtained was washed several times in deionized water, dialyzed and dried for further studies.

2.3 Cell culture and *E. coli* concentration optimization

Sample bacteria *E. coli* ATCC 25922 were collected from Aswini diagnostics, Calicut, Kerala, India. Microbiology Chromocult Coliform Agar from Merck was used as a medium. The sample was incubated at 37 °C for 24 hours to grow the bacteria. After

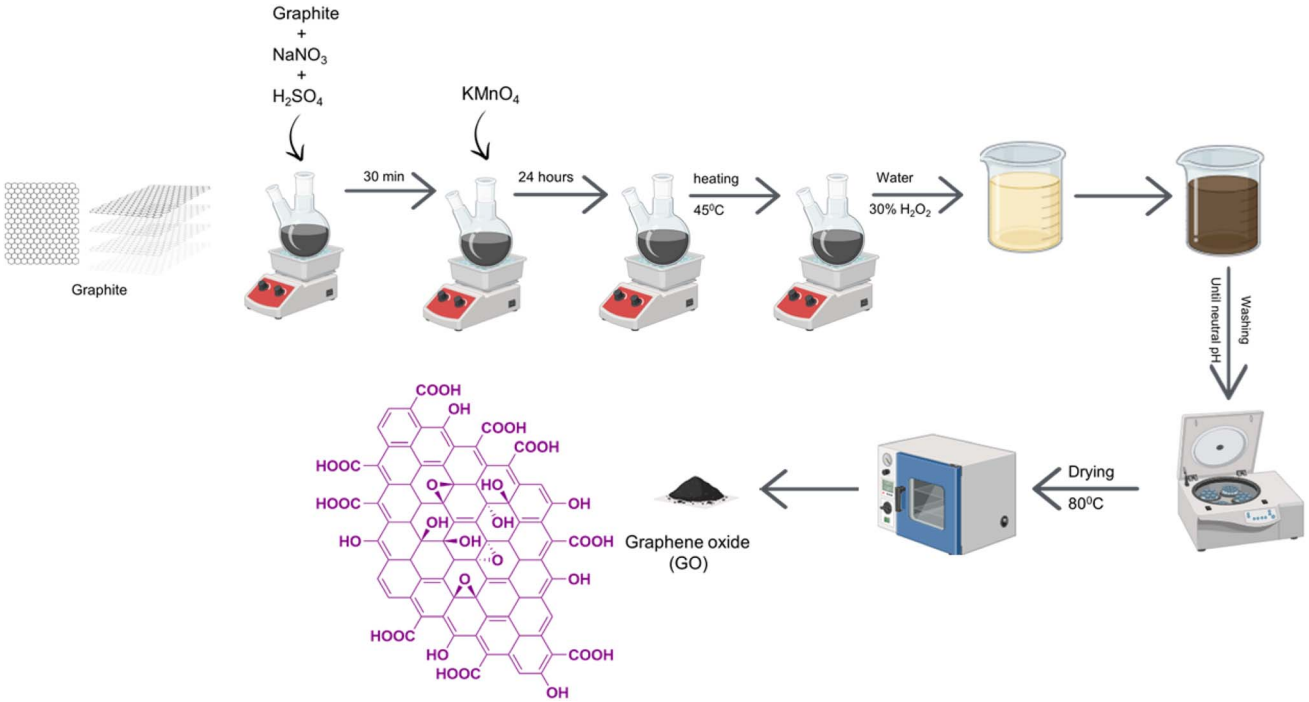

Fig. 1 Synthesis scheme of graphene oxide (GO). Created with Biorender.com.

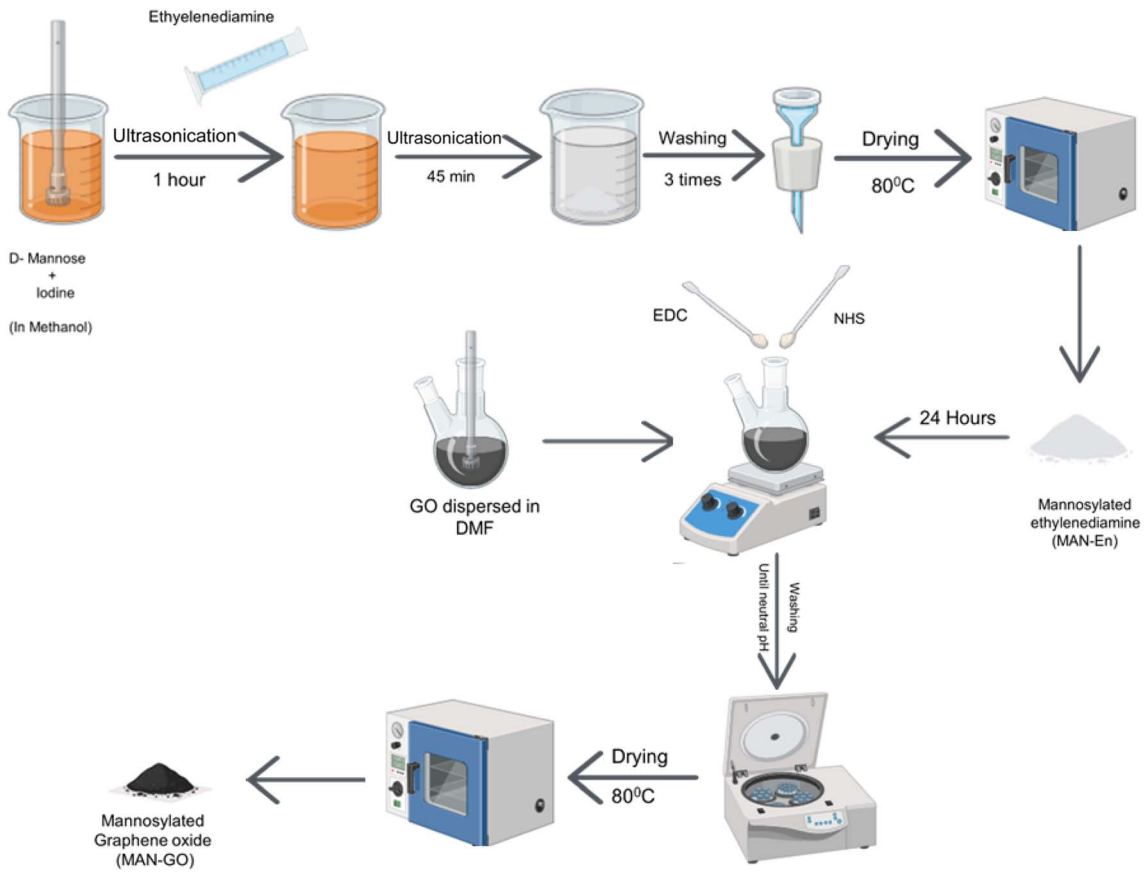

Fig. 2 Synthesis scheme of mannosylated graphene oxide (MAN-GO). Created with Biorender.com.

24 h incubation, a single colony of bacteria was isolated to new agar medium and further incubated at 37 °C for 24 hours. Then, the single colony was transferred to autoclaved liquid media, lysogeny broth (LB) at 37 °C, and the value of A_{600} was recorded.

2.4 Sample preparation for *E. coli* sensing studies and adsorption experiments

A 0.6 mg mL^{-1} solution of MAN-GO was dispersed in 1 mL of PBS buffer (pH 7.4) through 60 minutes of ultrasonication. The sample was then transferred to a cuvette, and *E. coli* sensing studies were conducted using a serial dilution method; after each addition, the sample was allowed to react for 1 minute. To evaluate the adsorption capacity of *E. coli* on MAN-GO, a series of *E. coli* solutions (7.25×10^8 CFU mL^{-1}, 6.84×10^8 CFU mL^{-1}, 5.64×10^8 CFU mL^{-1}, 5.10×10^8 CFU mL^{-1}, and 3.34×10^8 CFU mL^{-1}) were prepared *via* dilution. 5 mL of each solution was incubated with 0.6 mg mL^{-1} MAN-GO for 2 hours with stirring. The concentration of *E. coli* in the supernatant was examined using a UV-visible spectrometer. The amount of *E. coli* adsorbed was evaluated using the formula

$$q_e = \frac{(C_0 - C_e)V}{m} \quad (1)$$

where q_e = amount of *E. coli* per unit mass of adsorbent removed (CFU g^{-1}), C_0 and C_e are the initial concentration and equilibrium concentration of *E. coli* (CFU mL^{-1}), V is the volume of the solution (mL), and m is the amount of catalyst used (g). Percentage removal of *E. coli* was calculated using

$$\%\ \text{Removal of } E.\ coli = \frac{C_0 - C_t}{C_0} \times 100 \quad (2)$$

Different adsorption isotherm models were used to fit the experimental data. which are:

(a) Langmuir isotherm

$$\frac{C_e}{q_e} = \frac{1}{q_{max} K_L} + \frac{C_e}{q_{max}} \quad (3)$$

where K_L is the Langmuir constant and is consistent with the rate of adsorption (L g^{-1}) and q_{max} is the Langmuir maximum removal capacity of *E. coli* per unit mass of adsorbent (CFU g^{-1}). The separation factor R_L (dimensionless constant) can be used to determine the feasibility of the reaction given by the following equation: $R_L = \frac{1}{1 + (K_L C_0)}$.

(b) Freundlich isotherm

$$\ln q_e = \ln K_F + \frac{1}{n} \ln C_e, \quad (4)$$

where n and K_F are Freundlich constants indicating the adsorption favourability and adsorbent removal capacity. Adequate adsorption is indicated when the value of $1/n$ is between 0 and 1.

(c) Temkin isotherm

$$q_e = B \ln A + B \ln C_e \quad (5)$$

Table 1 Computed parameters for various adsorption isotherms and their corresponding correlation coefficients

Langmuir isotherm		Temkin isotherm	
Parameters	Value	Parameters	Value
Q_{max} (CFU g^{-1})	448.219	K_T (L CFU^{-1})	2.726×10^{-5}
K_L (L CFU^{-1})	2.9736	A (L CFU^{-1})	2.723×10^{-5}
R_L	4.638×10^{-9}	b (j mol^{-1})	1204.85
R^2	0.996	R^2	0.935
Freundlich isotherm		**D–R isotherm**	
Parameters	Value	Parameters	Value
K_F (CFU g^{-1})	5.336×10^6	Q_m (CFU g^{-1})	1.211×10^9
n	2.630	D	1.294×10^{-5}
$1/n$	0.380	E (kJ mol^{-1})	196.524
R^2	0.979	R^2	0.988

where C_e is the equilibrium concentration of the solution, A is the Temkin isotherm constant (L g^{-1}), B is the constant related to the heat of adsorption and equivalent to RT/b (b = Temkin constant (J mol^{-1}), T = absolute temperature (K), and R = gas constant (8.314 J mol^{-1} K^{-1})).

(d) Dubinin–Radushkevich model

$$\ln Q_e = \ln Q_m - D\varepsilon^2, \quad \varepsilon = RT \ln \left[\frac{(C_e + 1)}{C_e}\right] \quad (6)$$

where ε is the Polanyi potential. D and Q_m are the Dubinin constants and maximum adsorption capacity. Table 1 presents all the fitted parameters.

For the adsorption kinetic studies, the *E. coli* solution with a concentration of 1.352×10^7 CFU mL^{-1} was selected. It was incubated with 0.6 mg MAN-GO with stirring and the OD of the solution was recorded at 5 minute intervals. The adsorption kinetics of *E. coli* was followed using the equation

(a) Pseudo-first order

$$\ln(q_e - q_t) = \ln q_e - k_1 t \quad (7)$$

Here, q_t is the amount of *E. coli* adsorbed at time t and k_1 is the rate constant of the pseudo-first order equation:

(b) Pseudo-second order

$$\frac{t}{q_t} = \frac{1}{k_2 q_e^2} + \frac{t}{q_e} \quad (8)$$

where k_2 is the rate constant of the pseudo-second order equation:

(c) Elovich model

$$q_t = \left(\frac{1}{(\beta \ln[\alpha\beta])}\right) + \left(\frac{1}{(\beta \ln[t])}\right) \quad (9)$$

in which α is the initial adsorption rate (CFU g^{-1} min^{-1}) and β is a constant related to the extent of surface coverage and activation energy at time (t) adsorbed.

(d) Intraparticle diffusion model

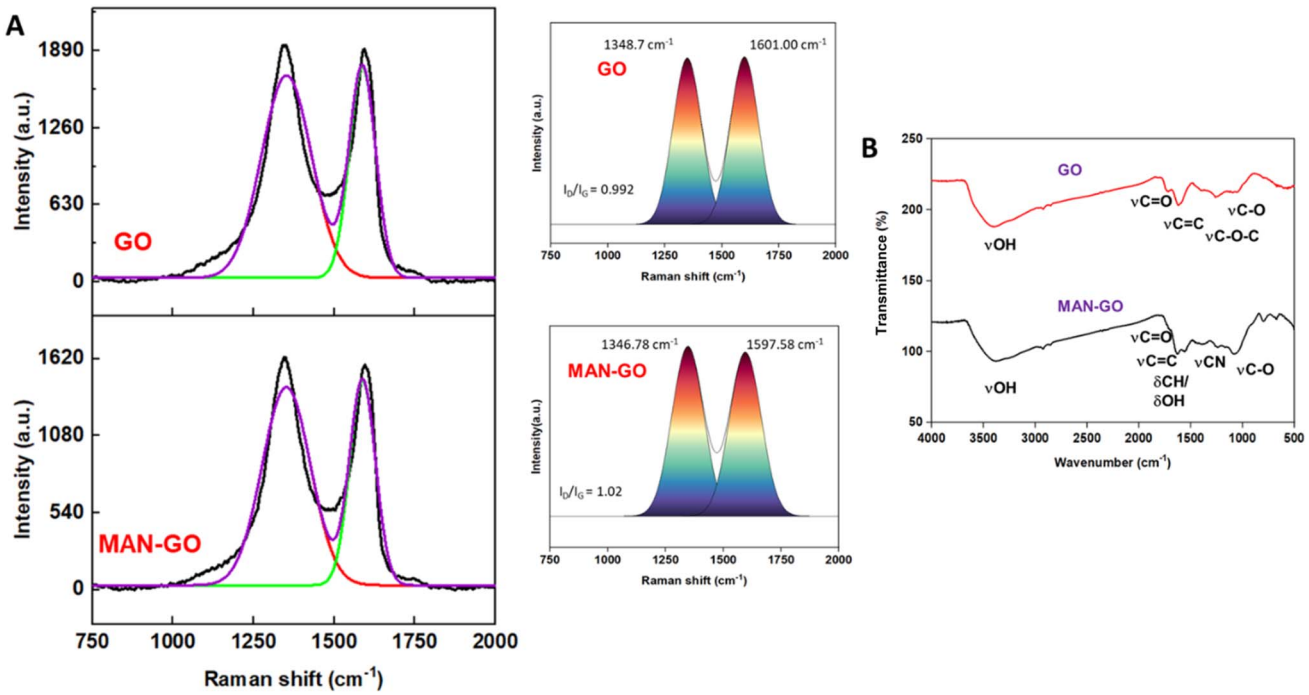

Fig. 3 (A) Deconvoluted Raman spectra of GO and MAN-GO showing the D and G bands, highlighting structural changes upon mannose functionalization. (B) FTIR spectra of GO and MAN-GO indicating the presence of characteristic functional groups and confirming successful mannose conjugation. Spectra were recorded at room temperature with a scan range of 4000–400 cm^{-1}.

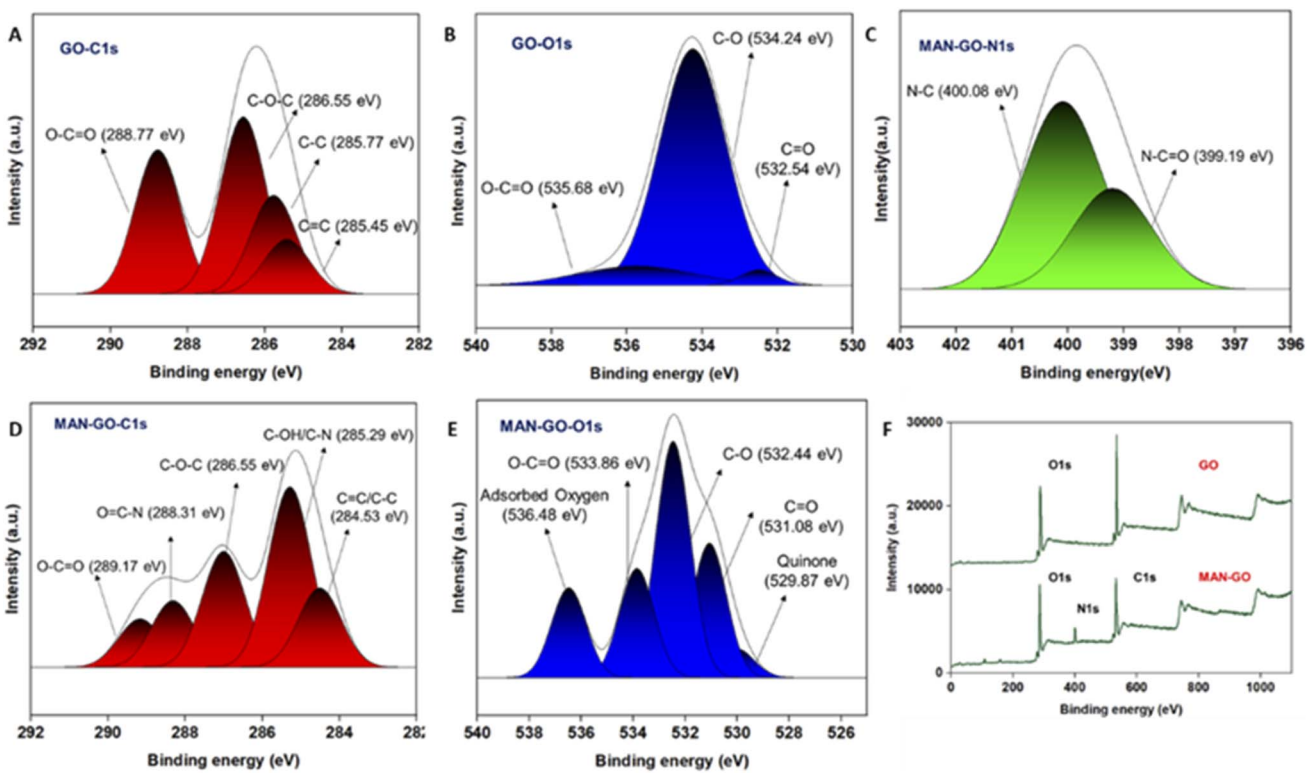

Fig. 4 XPS analysis of GO and MAN-GO composites: (A) high-resolution C 1s spectrum of GO showing the carbon bonding states; (B) high-resolution O 1s spectrum of GO; (C) N 1s spectrum of MAN-GO confirming the presence of nitrogen due to mannose functionalization; (D) C 1s spectrum of MAN-GO showing shifts in binding energies upon functionalization; (E) O 1s spectrum of MAN-GO; (F) survey spectra of GO and MAN-GO showing elemental composition and successful incorporation of nitrogen in MAN-GO.

$$q_t = k_p(t^{1/2}) + C \quad (10)$$

where k_p is the intraparticle diffusion rate constant and C is the boundary layer thickness (mg g^{-1}).

2.5 Cell culture for cytotoxicity evaluation

L929 mouse fibroblast cells were procured from NCCS Pune and cultured in 25 cm^2 tissue culture flasks using DMEM supplemented with 10% FBS, L-glutamine, sodium bicarbonate, and antibiotics (Penicillin 100 U mL^{-1}, Streptomycin 100 μg mL^{-1}, and Amphotericin B 2.5 μg mL^{-1}). The cells were maintained at 37 °C in a humidified 5% CO_2 incubator. Cell viability was initially assessed *via* phase-contrast microscopy and further confirmed using the MTT assay. For testing, confluent cells were trypsinized and seeded at a density of 5×10^3 cells/well in 96-well plates. A 1 mg sample was dissolved in 1 mL DMEM using a cyclomixer, filtered through a 0.22 μm syringe filter, and used for further treatment.

2.6 Cytotoxicity evaluation *via* microscopic observation and MTT assay

After 24 hours of cell seeding, the growth medium was removed, and test compounds were added at concentrations of 100, 50, 25, 12.5, and 6.25 μg mL^{-1} in DMEM, with each concentration tested in triplicate. Untreated control cells were also maintained. Cytotoxic effects were initially assessed through direct microscopic observation using an inverted phase-contrast microscope (Olympus CKX41 with Optika Pro5 CCD camera), noting morphological changes such as cell rounding, shrinkage, granulation, and vacuolization as indicators of cytotoxicity. For quantitative assessment, the MTT assay was performed by reconstituting 15 mg MTT in 3 mL PBS, filter sterilizing the solution, and adding 30 μL to each well after removing the treatment medium. Plates were incubated at 37 °C for 4 hours, followed by the addition of 100 μL DMSO to solubilize the formazan crystals. Absorbance was recorded at 540 nm using a microplate reader, and the percentage of growth inhibition was calculated using the formula

$$\%\ \text{Inhibition} = \frac{\text{mean OD of samples}}{\text{mean OD of control group}} \times 100$$

3 Results and discussion

3.1 Characterization of GO and MAN-GO

In this study, we employed D-mannose modified GO, which has been synthesized through covalent functionalization, a method previously reported in the literature.[31,34] The covalent functionalization was performed using EDC and NHS chemistry, where sheet-like graphene oxide was covalently linked to mannosylated ethylenediamine.

The IR patterns of the synthesized GO and MAN-GO show a broad and intense band with a maximum at 3390 cm^{-1}, which is typically attributed to the O–H stretching vibration (Fig. 3B). All peaks are consistent with the reported peaks in the literature. The band observed at 1705 cm^{-1}, for GO, has been assigned to the C=O stretching from carboxylic acid groups, with a reduction in intensity, after conversion to an amide bond.[35] The remaining small band at this position is likely due

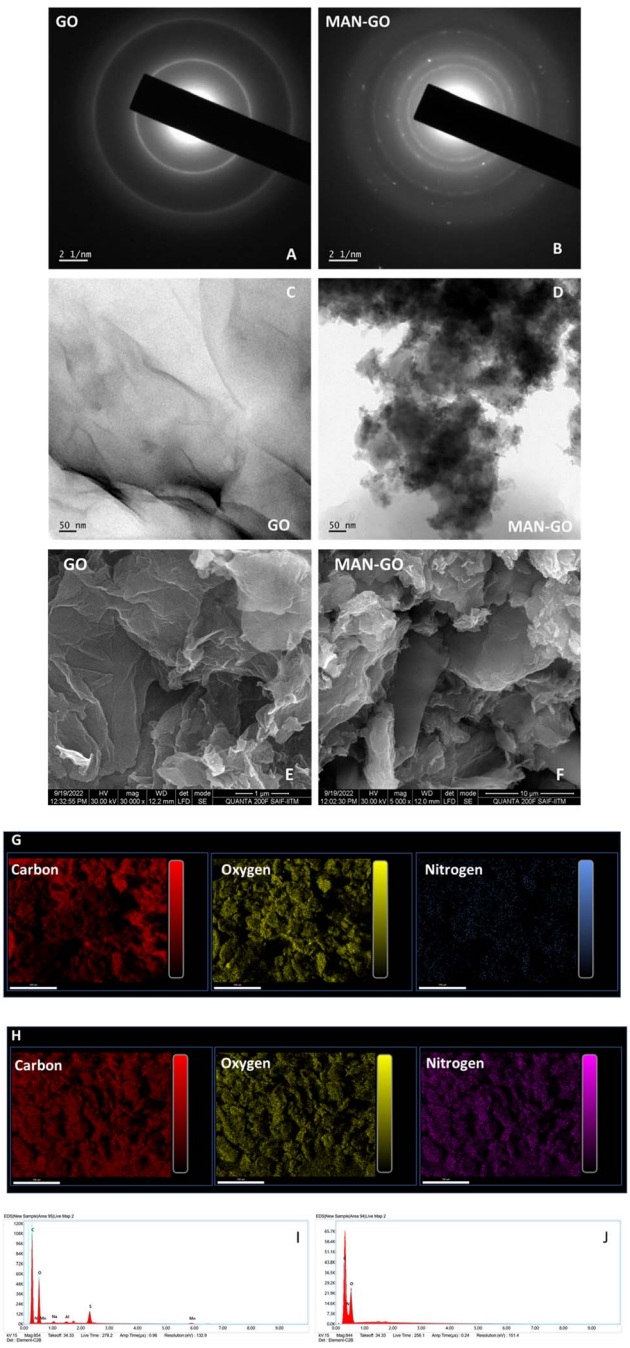

Fig. 5 Structural and compositional characterization of graphene oxide (GO) and mannosylated graphene oxide (MAN-GO). (A) Selected Area Electron Diffraction (SAED) pattern of GO, (B) SAED pattern of MAN-GO, (C) transmission electron microscopy (TEM) image of GO, (D) TEM image of MAN-GO, (E) scanning electron microscopy (SEM) image of GO, (F) SEM image of MAN-GO, (G) Energy Dispersive X-ray Spectroscopy (EDS) elemental mapping of GO, (H) EDS elemental mapping of MAN-GO, (I) corresponding EDS spectrum of GO, and (J) corresponding EDS spectrum of MAN-GO.

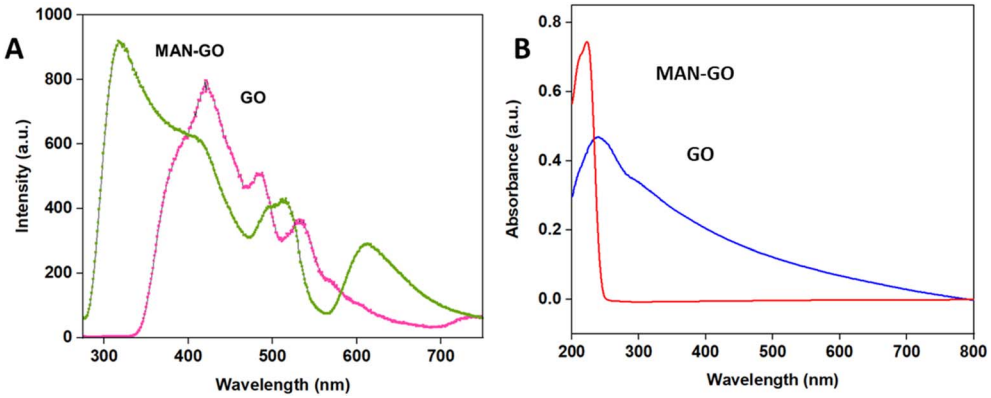

Fig. 6 Optical characterization of graphene oxide (GO) and mannosylated graphene oxide (MAN-GO): (A) fluorescence emission spectra of GO and MAN-GO in a water/ethanol mixture at a 20 nm slit width and 250 and 220 nm excitation wavelength; (B) UV-Vis absorption spectra of GO and MAN-GO in water.

to the presence of ketone groups. The C═O stretching of the amide bond overlaps with the C═C bond of the graphene oxide network, both appearing at 1628 cm^{-1}. Additionally, two distinct bands are observed at 1381 cm^{-1} and 1237 cm^{-1}, corresponding to the CH/OH and amine CN stretching vibrations of MAN-En, respectively. The strong band at 1068 cm^{-1} is attributed to the C–O stretching, which includes contributions from the CO bonds in MAN-En. The clear and distinct signals

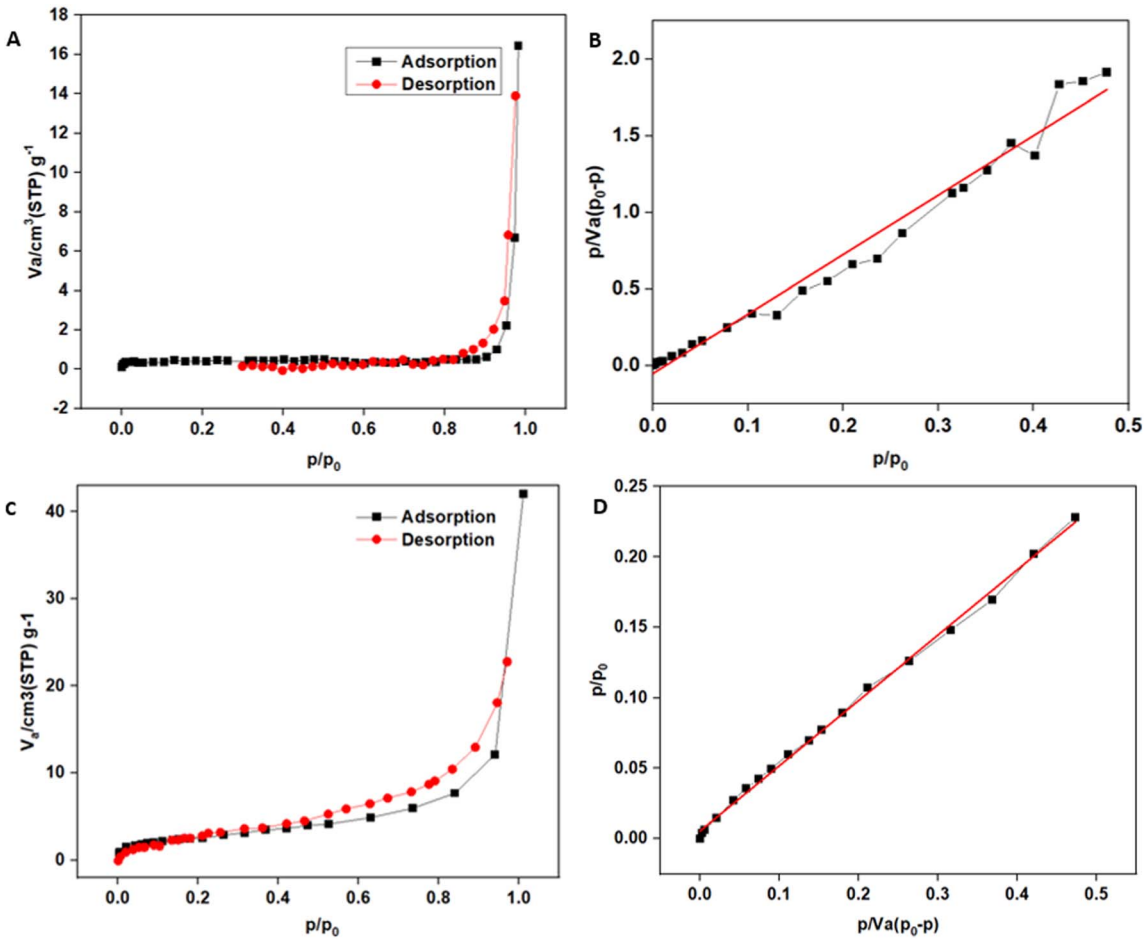

Fig. 7 Porosity and surface area analysis of graphene oxide (GO) and mannosylated graphene oxide (MAN-GO). (A) Nitrogen adsorption–desorption isotherms of MAN-GO, (B) Brunauer–Emmett–Teller (BET) surface area plot of MAN-GO, (C) nitrogen adsorption–desorption isotherms of GO, and (D) BET surface area plot of GO.

associated with the sugar indicate that the MAN-En was successfully conjugated to the GO.[36,37] The Raman spectrum of pristine GO exhibited two primary bands: the D band at 1348.7 cm^{-1} and the G band at 1601.00 cm^{-1}, resulting in an intensity ratio I_D/I_G of 0.992 (Fig. 3A). In graphene-based materials, the D band is associated with the presence of defects, disorder, and the breathing modes of sp^2 carbon rings, while the G band corresponds to the in-plane vibrational mode of sp^2-hybridized carbon atoms.[37] Upon functionalization, the Raman spectrum of MAN-GO showed a slight downshift in the D band to 1346.78 cm^{-1} and in the G band to 1597.58 cm^{-1}, accompanied by a modest increase in the I_D/I_G ratio to 1.02. The downshift in both the D and G bands suggests alterations in the electronic environment and the sp^2 network of GO, likely due to the covalent attachment of MAN-En.[34] Furthermore, the higher defect density, attributed to the introduction of additional functional groups during the mannosylation process, offers promising evidence for the functionalization.

The coupling of D-mannose to GO has been further confirmed by XPS analysis. The deconvolutions and attributions were derived from previously published studies.[38–42] The survey and high-resolution XPS data are presented in Fig. 4A–F. Fig. 2F displays the survey observations indicating the presence of carbon, oxygen, and nitrogen in MAN-GO, while only carbon and oxygen are present in GO. The existence of nitrogen in MAN-GO implies the formation of a covalent bond between MAN-En and GO. Transmission electron microscopy and scanning electron microscopy have been used to demonstrate the morphological characteristics of GO and MAN-GO. A selected area electron diffraction (SAED) pattern from the monolayer region of GO and MAN-GO is shown in Fig. 5A and B, respectively. GO exhibits folded sheet-like structures, whereas MAN-GO appears to be more aggregated and irregular, reflecting the changes due to mannose functionalization. The SAED pattern of GO shows its polycrystalline nature (Fig. 5A), while that of MAN-GO, shown in Fig. 5B, clearly indicates crystalline nature with multiple crystal diffraction patterns. The quantitative identification and elemental composition of GO and MAN-GO were further executed by EDS (Fig. 5G and H). The presence of carbon and oxygen in GO is clearly reflected in the EDS spectrum. In the MAN-GO elemental spectrum, the peak corresponding to nitrogen is more evident in addition to carbon and oxygen, which demonstrates the successful combination of mannose on GO.

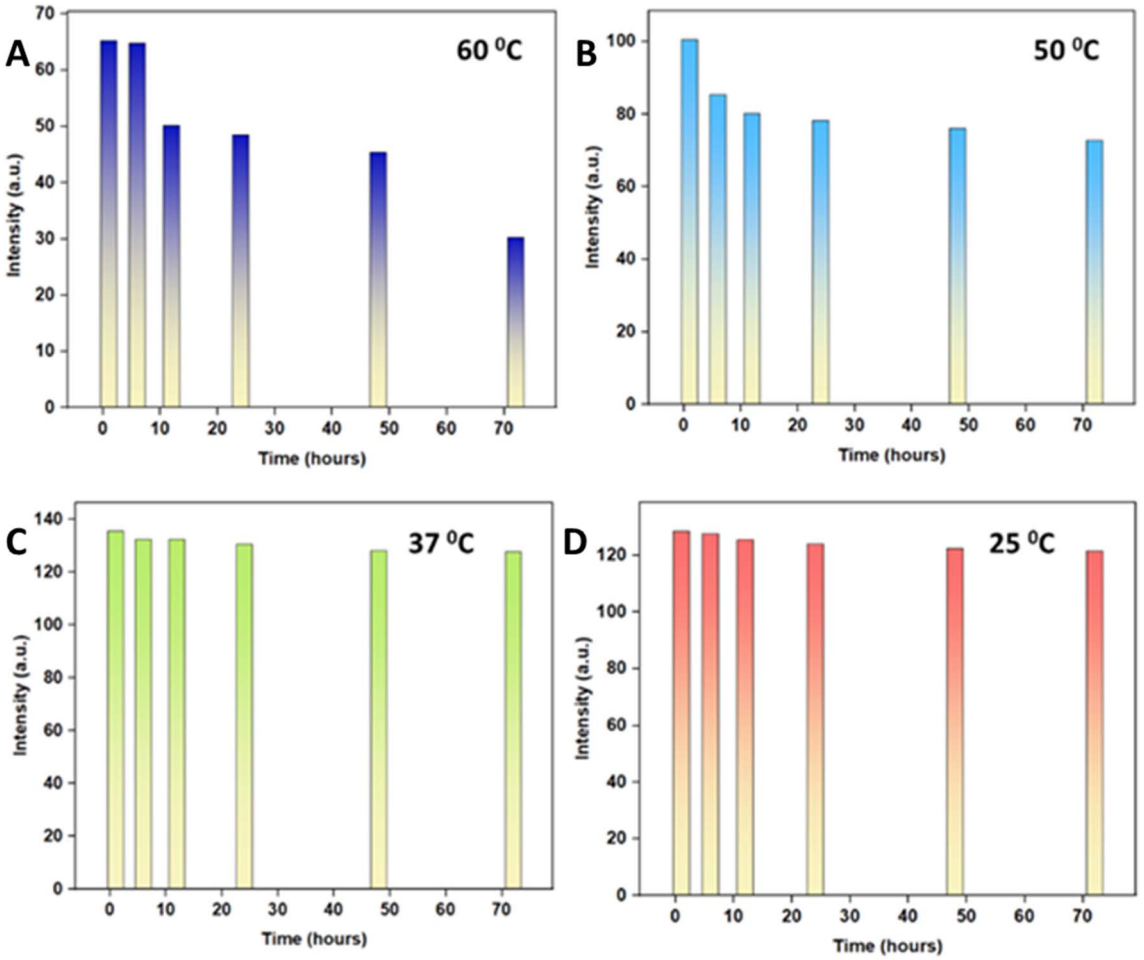

Fig. 8 *E. coli* binding efficacy and stability of the tested material at various temperatures. Fluorescence measurements were recorded in PBS buffer with an excitation wavelength of 250 nm and a 10 nm slit width. (A) 60 °C, (B) 50 °C, (C) 37 °C, and (D) 25 °C.

The fluorescence phenomenon is attributed to the recombination of electrons and holes occurring between the lower edge of the conduction band, adjacent localized states, and the expansive valence band. Applying molecular orbital theory, it has been determined that the primary fluorescence results from electronic transitions within and between non-oxidized carbon areas and the periphery of the oxidized carbon regions. This process involves the participation of three functional groups: C–O, C═O, and O═C–OH.[43] The fluorescent properties of GO and MAN-GO have been evaluated in an ethanol/water mixture. Measurements were done at an excitation wavelength of 250 nm, with the emission spectra recorded across a range from 270 nm to 750 nm (Fig. 6A) The UV-visible spectra of GO and MAN-GO reveal distinct absorption features arising from the π–π* transitions of C═C bonds and the n–π* transitions of C═O groups (Fig. 6B). Upon mannose functionalization, a noticeable shift and intensity variation are observed, confirming successful surface modification of GO. These spectral changes further validate the alteration in the electronic structure and surface chemistry after glyco-functionalization.[44]

The specific surface area and porosity of GO and its derivatives significantly influence their applications in adsorption,[45] sensing,[46,47] and catalysis.[48] To evaluate the effect of mannose functionalization on the surface properties, BET analysis has been performed on pristine GO and MAN-GO. BET surface area measurements were conducted using a BELSORP high precision gas/vapour adsorption apparatus. Samples were degassed at 120 °C under vacuum for 3 hours before analysis to remove adsorbed moisture and impurities. Nitrogen adsorption–desorption isotherms were recorded at 77 K over a relative pressure range. The nitrogen adsorption–desorption isotherms of GO and MAN-GO (Fig. 7) exhibit Type II behavior, identifying them as relatively strong materials. The BET-specific surface area of GO was determined to be 14.487 $m^2 g^{-1}$, while MAN-GO exhibited a reduced surface area of 1.4521 $m^2 g^{-1}$ from the equation

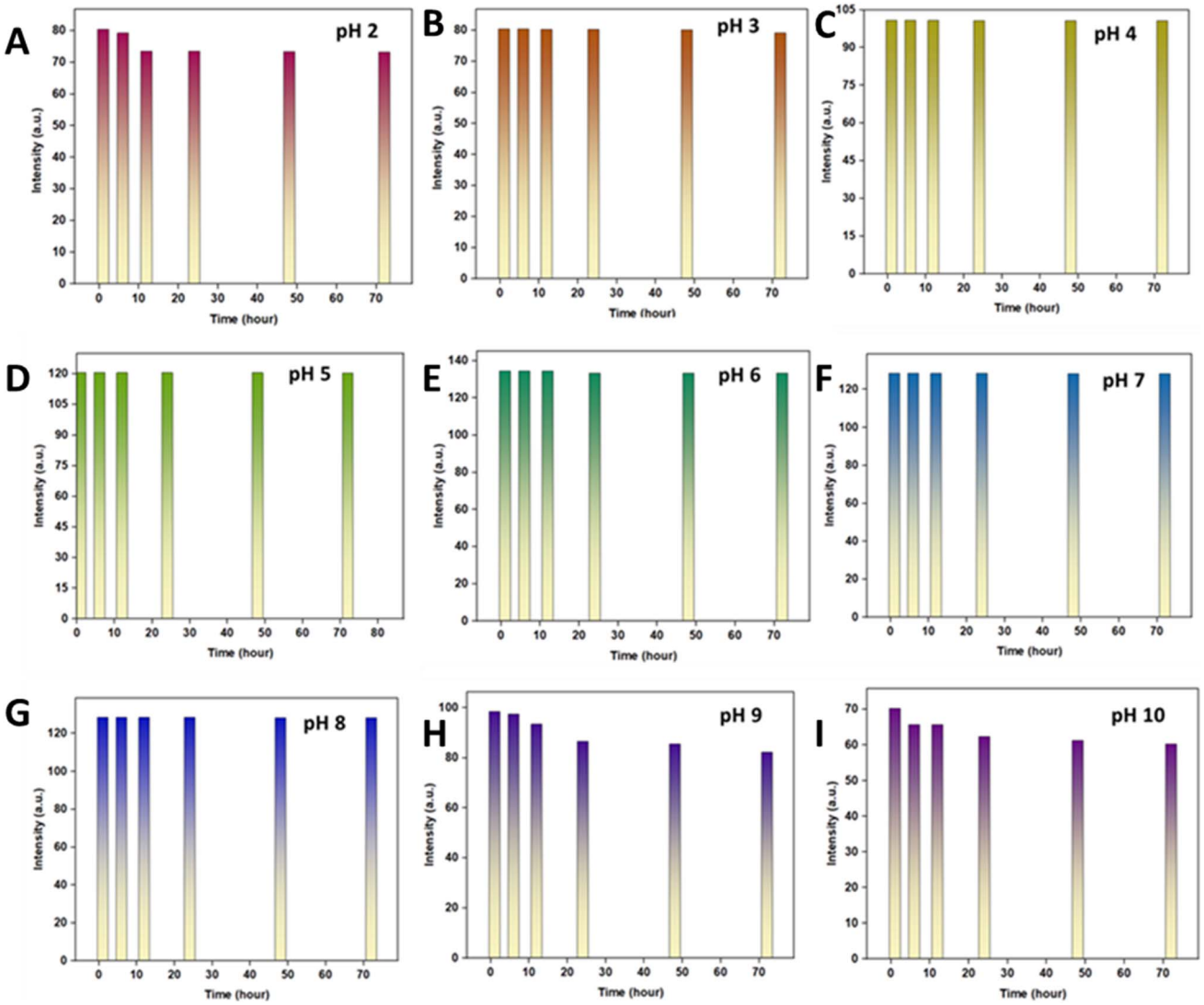

Fig. 9 *E. coli* binding efficacy and stability of the material at varying pH levels. Fluorescence measurements were performed in PBS buffer with an excitation wavelength of 250 nm and a slit width of 10 nm: (A) pH 2, (B) pH 3, (C) pH 4, (D) pH 5, (E) pH 6, (F) pH 7, (G) pH 8, (H) pH 9, and (I) pH 10.

$$a_s = \frac{V_m}{22\,414} \times L \times \sigma \quad (11)$$

where V_m is the monolayer volume, L the Avogadro constant, and σ the cross-sectional area of an adsorbate molecule. σ is defined as the average area that one adsorbed molecule occupies on the solid surface, which is calculated under the assumption that adsorbed molecules form the closest packing on a solid surface.

On the other hand, MANGO, with its larger mean pore diameter (70.047 nm) and substantially higher C constant (2910.5), provides enhanced adsorbent–adsorbate interactions and facilitates the capture of larger molecular or cellular entities such as *E. coli*. The mannose functionalization enhances selectivity and interaction strength, positioning MAN-GO as a more effective material for microbial sensing and adsorption in biomedical and environmental applications. These results demonstrate that functionalization can significantly improve the performance of GO. The detailed parameters, including surface area, pore size, and adsorption constants, are given in Tables S3 and S4.

3.2 Optimization and fabrication of the sensing probe

The concentration of MAN-GO was optimized as 0.6 mg mL^{-1} by repeated fluorescence measurement experiments in PBS buffer (pH 7.4). To assess the stability and binding efficacy of *E. coli* towards MAN-GO, the fluorescence spectra were recorded at different temperatures (60 °C, 50 °C, 37 °C, and 25 °C) and different pH (2 to 10) with 0.6 mg mL^{-1} MAN-GO in 1 mL *E. coli* solution with a concentration of 10^5 CFU mL^{-1} at different time intervals (Fig. 8 and 9).

Among different temperatures, the maximum binding efficacy by *E. coli* to MAN-GO was observed at 37 °C and pH 7. The optimal binding efficacy of *E. coli* to MAN-GO at 37 °C and pH 7 corresponds to the natural physiological environment of *E. coli*, where it maintains optimal cellular function and membrane integrity. At this temperature and pH, the bacterial surface structures, such as mannose receptors, are more accessible and interact effectively with mannose-functionalized graphene oxide, with enhanced binding affinity.[49,50]

It is well established that *E. coli*, when excited with light at 250 nm, exhibits a characteristic fluorescence emission peak in the range of 330–350 nm, primarily due to the intrinsic fluorescence of tryptophan residues in bacterial proteins. Other aromatic amino acids and nucleic acids can also contribute to a broader fluorescence profile spanning 280–480 nm.

In view of this, we carefully recorded the fluorescence spectra of *E. coli* alone under different excitation wavelengths as

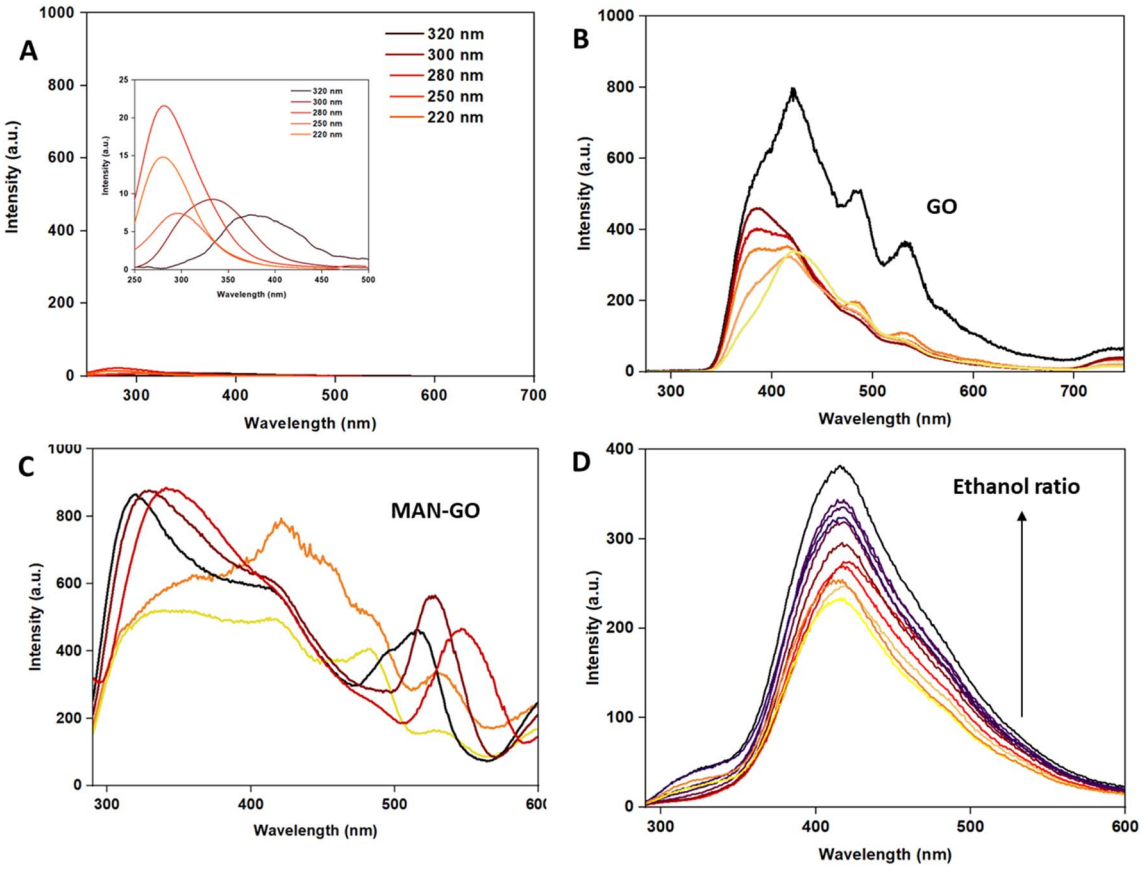

Fig. 10 (A) Intrinsic fluorescence emission spectra of *E. coli* at different excitation wavelengths (220–320 nm). Inset: zoomed-in view showing the low-intensity emission profiles. (B) Fluorescence spectra of GO under various excitation wavelengths, showing strong emission features. (C) Fluorescence spectra of MAN-GO under different excitation wavelengths, indicating altered optical properties upon mannose functionalization. (D) Effect of the ethanol ratio on fluorescence spectra, demonstrating gradual intensity variations with increasing ethanol content.

a control (Fig. 10A). The results confirmed that the intrinsic fluorescence intensity of *E. coli* was very low compared to the signals observed in the sensing experiments. This indicates that the strong fluorescence response in our system predominantly arises from the interaction of *E. coli* with MAN-GO, rather than from the intrinsic fluorescence of the bacteria. The fluorescence of GO and MAN-GO, varying based on excitation wavelength, was assessed in aqueous solutions using different wavelengths ranging from 220 nm to 300 nm (Fig. 10B and C). The fluorescence of GO primarily arises from π–π* transitions within its sp^2-hybridized carbon domains, while the presence of oxygen-containing functional groups such as –COOH and –OH influences its emission properties by modifying the electronic structure and local environment. These groups contribute to broad and excitation-dependent emission, particularly at low to neutral pH, due to changes in surface chemistry, defect states, and intermolecular interactions, features that make GO suitable for chemical sensing and bioimaging applications. The fluorescence of GO has been examined across different ethanol–water ratios, with a noticeable increase in emission intensity (Fig. 10D). The increase in emission intensity of GO in higher ethanol–water ratios is likely due to reduced hydrogen bonding with water molecules, which can suppress fluorescence. Moreover, ethanol may also induce changes in GO's electronic structure or stabilize excited states, enhancing fluorescence.

3.3 Cell viability

Both GO and MAN-GO exhibited minimal cytotoxic effects on L929 fibroblast cells at lower concentrations, maintaining cell viability above 90% at doses below 12.5 μg mL^{-1}. At elevated concentrations, cell viability decreased moderately to approximately 76% for GO and 77% for MAN-GO, indicating only moderate cytotoxicity (Fig. 11).

The LC_{50} values were determined to be 212.95 μg mL^{-1} for GO and 228.99 μg mL^{-1} for MAN-GO, further demonstrating their favorable biocompatibility. These results suggest that both nanomaterials possess a relatively high safety margin, with significant cytotoxic effects manifesting only at concentrations

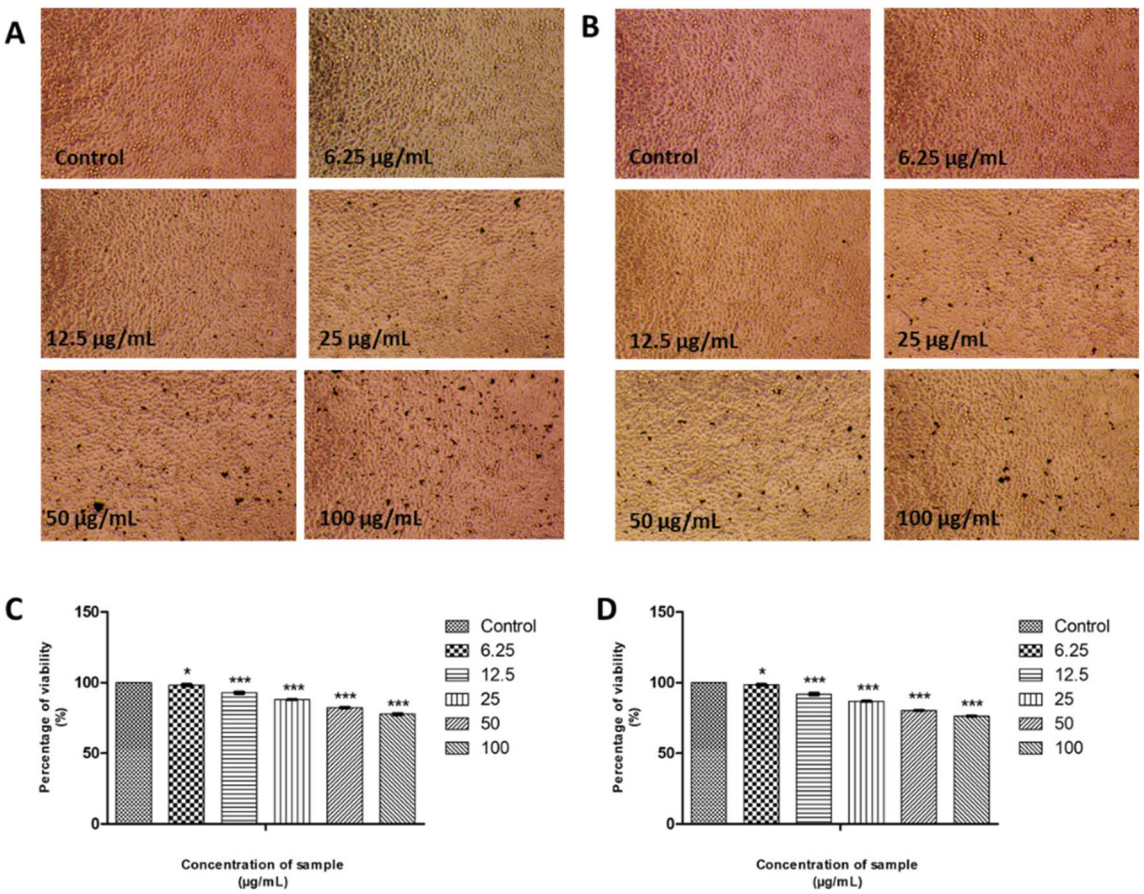

Fig. 11 (A) The inverted phase contrast tissue culture microscope images after 24 hours of treatment using MAN-GO, (B) the inverted phase contrast tissue culture microscope images after 24 hours of treatment using MAN-GO, and (C) graphical representation depicting the cytotoxic effect of GO by MTT assay; *Y* axis represents percentage viability and *X* axis represents varying concentrations of GO. All experiments were done in triplicate and results are presented as Mean ± SE. One-way ANOVA and Dunnett's test were performed to analyse data. ***$p < 0.001$ compared to the control group and *$p < 0.1$ compared to the control group. (D) Graphical representation depicting the cytotoxic effect of GO determined by MTT assay; *Y* axis represents percentage viability and *X* axis represents varying concentrations of GO. All experiments were done in triplicate and results are presented as Mean ± SE. One-way ANOVA and Dunnett's test were performed to analyse data. ***$p < 0.001$ compared to the control group and *$p < 0.1$compared to the control group.

substantially exceeding those relevant for biomedical applications. Notably, mannose functionalization did not exacerbate cytotoxicity; rather, MAN-GO exhibited a slightly higher LC_{50} value, indicative of marginally enhanced cellular compatibility. The observed cytotoxicity at higher doses may be attributed to nanoparticle internalization and subsequent reactive oxygen species (ROS) generation, leading to oxidative stress. Nevertheless, the moderate decrease in cell viability at elevated concentrations does not detract from the overall potential of GO and MAN-GO for safe use.

3.4 Sensing studies

The *E. coli* sensing studies were carried out by dispersing 0.6 mg of MAN-GO in 1 mL of PBS. The bacterial cells were precultured, and their concentrations were quantified using OD measurements. Fluorescence measurements were then performed by varying the bacterial concentration in the range of 0 to 10^9 CFU mL^{-1}. At lower concentrations, 0–10^3 CFU mL^{-1}, no significant variation in emission intensity was observed, indicating minimal interaction between MAN-GO and the bacterial cells at this stage. However, beyond 10^3 CFU mL^{-1}, a clear increase in emission intensity was recorded, followed by a gradual decrease at higher bacterial concentrations. This trend suggests that MAN-GO exhibits a concentration-dependent sensing response, with an optimal range of bacterial detection occurring beyond 10^3 CFU mL^{-1}. For the recyclability studies, the emission spectrum of MAN-GO incubated with a 9.5×10^5 CFU mL^{-1} *E. coli* solution was first recorded. Then, MAN-GO was sonicated for 30 minutes, washed three times, and centrifuged. The same material was subsequently re-incubated with *E. coli*, and the spectra were recorded again. This process was repeated for a total of 13 cycles (Fig. 12B). The material exhibited good stability up to four cycles, maintaining its fluorescence intensity with minimal decrease. However, the quenching of fluorescence intensity observed after each cycle beyond the fourth is attributed to the binding of *E. coli* to the MAN-GO composite. The observed decrease in the fluorescence signal with increasing bacterial concentration is likely due to fluorescence quenching caused by interactions between the MAN-GO probe and the bacterial cell surface. Specifically, components on the bacterial

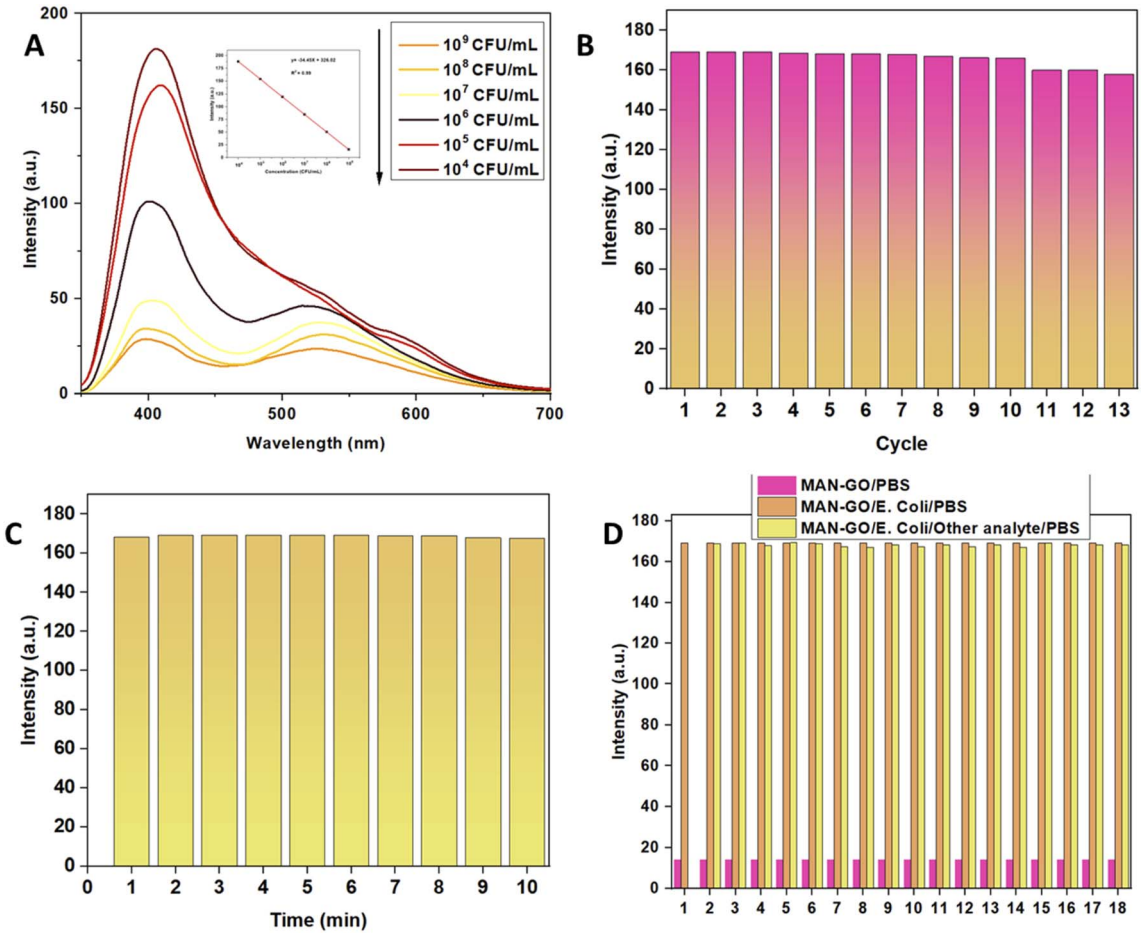

Fig. 12 Performance evaluation of the sensor system for *E. coli* detection. (A) Effect of varying *E. coli* concentration on fluorescence intensity. (B) Recyclability of the sensor over multiple detection cycles. (C) Response time analysis indicating the sensor's detection speed. (D) Fluorescence response of MAN-GO, MAN-GO/*E. coli* and MAN-GO/*E. coli* in the presence of various potential interferents. The graph displays numbered groups (1–18), each representing a specific analyte or ion tested for its effect on fluorescence intensity. For clarity, the detailed composition of each group is provided in the SI (Table S7).

outer membrane, such as lipopolysaccharides and membrane proteins, may facilitate non-radiative energy transfer or induce aggregation of the MAN-GO nanosheets. This aggregation or close contact between the probe and bacterial surface leads to a reduction in fluorescence emission intensity. Additionally, the adsorption of the probe onto the bacterial surface may result in static or dynamic quenching mechanisms, reducing the overall fluorescence signal. This behavior is consistent with previous reports of fluorescence quenching upon binding of fluorescent probes to bacterial surfaces.[51,52] As the bacteria bind to the composite, they may alter or quench the fluorescence emission, and this effect may become more pronounced with repeated cycles. Additionally, the gradual loss of the MAN-GO material during washing, sonication, and centrifugation could further reduce the composite's ability to interact with *E. coli*. Accumulation of residual bacteria or contaminants on the surface may also interfere with the fluorescence signal, contributing to the observed decrease in intensity. The response time of the analyte was evaluated, and a stable fluorescence signal was observed within 2 minutes (Fig. 12C). Potential interference from other components was assessed by recording the fluorescence spectra of MAN-GO in the presence of *E. coli* and various other analytes (Fig. 12D). Among the tested analytes, the strongest and most distinct signal has been obtained for *E. coli*, confirming the specificity of the MAN-GO composite.

To further evaluate the sensing mechanism, additional control experiments were performed. In particular, the intrinsic absorption (Fig. S3) and fluorescence of *E. coli* were recorded at varying excitation wavelengths, which confirmed the possibility of partial overlap with the MAN-GO excitation/emission windows. This overlap highlights the contribution of the IFE in modulating the observed fluorescence signal. However, as shown in Fig. 14B, GO without mannose functionalization exhibits an inherently very low fluorescence intensity. Because of this weak baseline signal, the extent of fluorescence modulation arising from IFE is expected to be very low. Therefore, the strong and concentration-dependent fluorescence quenching observed exclusively with MAN-GO cannot be attributed to IFE alone. This enhanced response is predominantly governed by the specific mannose-fimbriae recognition and subsequent bacterial adsorption on the MAN-GO surface, with IFE playing only a minor supporting role.

3.5 Real sample analysis

To evaluate the presence of *E. coli* and its interaction with MAN-GO, water samples were collected from various locations within the Calicut region, including the Kallai River, Canoli Canal, and Puthiya Palam. Each 1 mL sample was treated with 0.6 mg of MAN-GO and subsequently incubated to assess *E. coli* binding. Fluorescence analysis was performed under identical experimental conditions to detect *E. coli* concentrations across three samples, each spiked with a known concentration of the bacteria. The fluorescence spectra (Fig. 13) revealed variations in intensity among the different samples (Samples 1–3), corresponding to the differences in bacterial concentrations. This underscores the effectiveness of MAN-GO in capturing and detecting *E. coli* from diverse water matrices, further demonstrating its potential as a reliable biosensing material.

To validate the accuracy and robustness of the MAN-GO-based detection system, recovery rates were calculated for each water sample. The recovery rate was determined using the formula

$$\text{Recovery rate } (\%) = \frac{\text{concentration detected(after spiking)}}{\text{concentration spiked}} \times 100 \quad (12)$$

The calculated recovery rates for the three samples were 100.71%, 100.9%, and 101.3%, respectively. The results highlight the high sensitivity and accuracy of the MAN-GO-based detection platform, even in the presence of complex water matrices. The minimal deviation from the expected values also demonstrates its potential for real-world applications in environmental monitoring and water quality assessment.

3.6 Evaluation of specificity of MAN-GO

To strengthen the conclusions of our study, we have systematically tested non-functionalized GO and glucosylated GO under

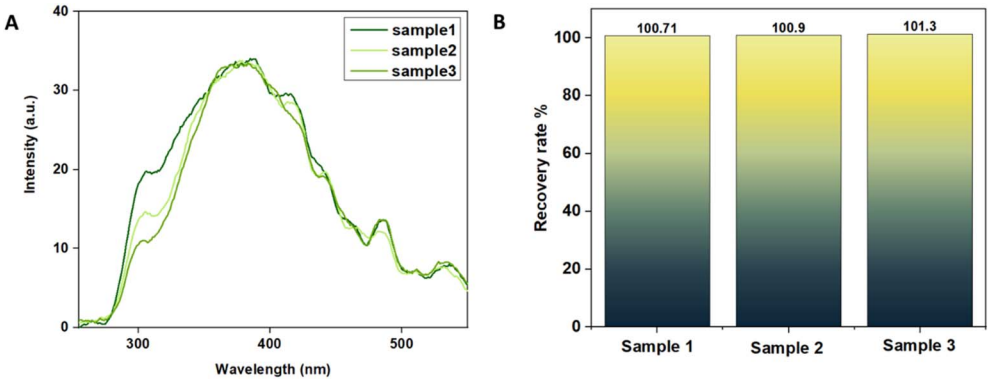

Fig. 13 Fluorescence analysis of real water samples using the MAN-GO composite sensor. (A) Variation in fluorescence intensity of water samples collected from different localities. (B) Recovery rate analysis of spiked analytes in real water samples using the MAN-GO composite.

the same experimental conditions, using the same strategy, to confirm that the enhanced fluorescence response is specifically due to the mannose functionalization rather than from nonspecific or general carbohydrate effects. In Fig. 14, Graphs A and B present a comparative analysis of the fluorescence response of mannose-functionalized graphene oxide, non-functionalized GO, and glucosylated GO (GLU-GO) when interacting with *E. coli*. Graph A shows a bar chart comparing fluorescence intensity, where MAN-GO/*E. coli* exhibits significantly higher fluorescence compared to GO/*E. coli* and GLU-GO/*E. coli*. This result suggests that the mannose ligands on MAN-GO enable a specific and strong interaction with *E. coli* surface receptors, while the other materials display only minimal nonspecific adsorption. Graph B presents the fluorescence emission spectra of the three systems, further confirming that MAN-GO/*E. coli* produces a pronounced emission peak, whereas GO/*E. coli* and GLU-GO/*E. coli* show weak signals across the wavelength range. Graphs C and *D* further evaluate the selectivity of the MAN-GO nanosensor by comparing its response to different bacterial strains. Graph C shows a bar graph of fluorescence intensity when MAN-GO is incubated with *E. coli*, *Klebsiella*, and *S. aureus*. The results clearly indicate that MAN-GO exhibits a strong fluorescence response only in the presence of *E. coli*, while the signals for *Klebsiella* and *S. aureus* are minimal. This highlights the high selectivity of the MAN-GO nanosensor for *E. coli*, likely due to specific mannose–lectin interactions, which are not prominent in the other bacterial strains tested. Graph D presents the fluorescence spectra corresponding to these interactions, reinforcing the selectivity observation. The MAN-GO/*E. coli* system shows a strong and distinct emission peak, whereas the MAN-GO/*Klebsiella* and GLU-GO/*E. coli* systems display only low background signals across the measured wavelengths. These results demonstrate that the enhanced bacterial binding and fluorescence response are specifically attributable to the mannose functionalization, providing clear evidence that nonspecific interactions or other carbohydrate modifications, such as glucose, do not account for the observed effect, and further confirm that this enhanced response is not only mannose-dependent but also selective for bacterial strains expressing mannose-binding receptors, strongly supporting the targeted sensing capability of the MAN-GO nanosensor.

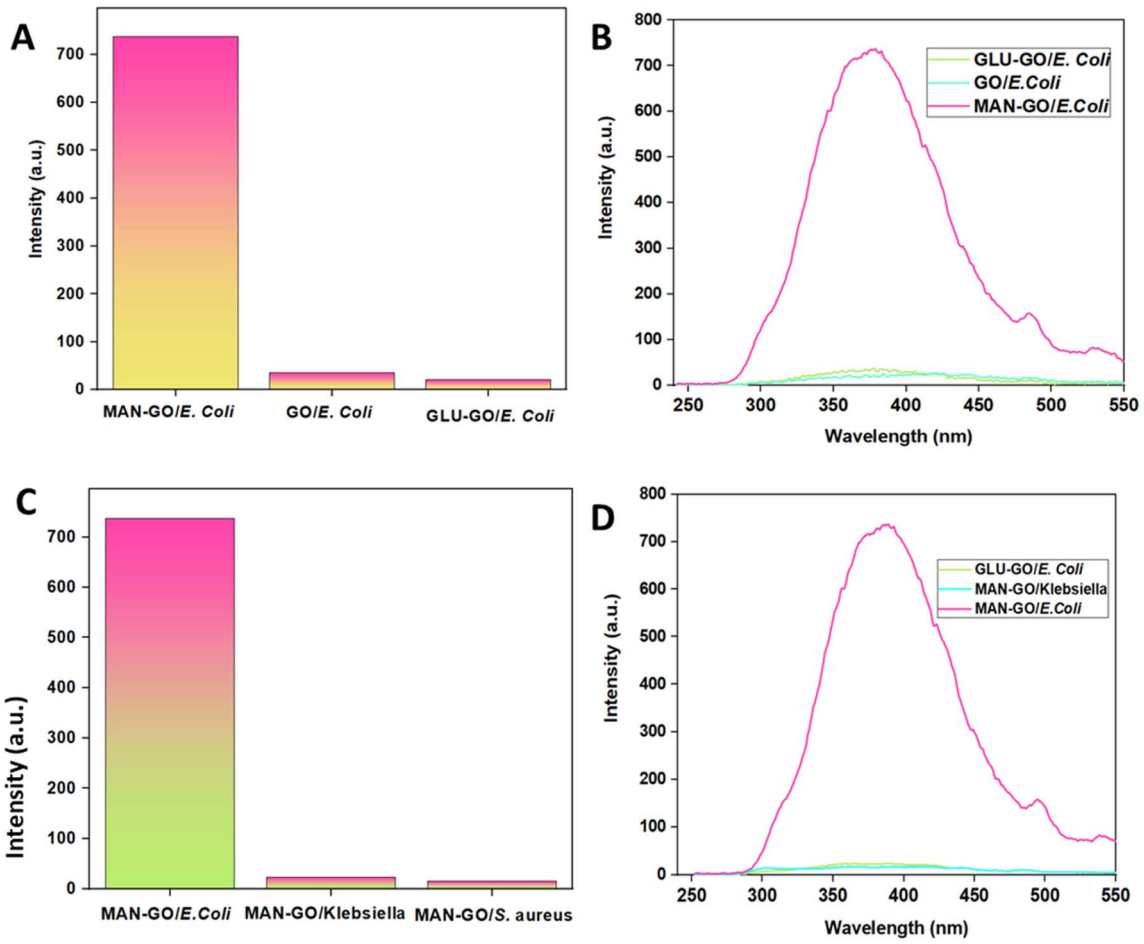

Fig. 14 Fluorescence response of mannose-functionalized graphene oxide (MAN-GO) toward bacteria. (A and B) MAN-GO shows significantly higher fluorescence intensity and spectra with *E. coli* compared to non-functionalized GO and glucosylated GO. (C and D) MAN-GO exhibits a selective fluorescence response toward *E. coli* over *Klebsiella* and *S. aureus*, confirming its mannose-mediated bacterial targeting.

3.7 Adsorption isotherm analysis

Adsorption isotherms are crucial for analysing the interaction between adsorbents and bacteria to offer valuable insights into adsorption capacity, surface characteristics, and the mechanism of bacterial removal.[53] Effective bacterial removal plays a vital role in mitigating environmental pollution and safeguarding public health by preventing the transmission of waterborne diseases. The Freundlich, Langmuir, Temkin, and Dubinin–Radushkevich (D–R) isotherms for bacterial adsorption onto MAN-GO at room temperature are presented in Fig. 13A to 13D. and the related parameters are given in Table 1.

Of all the models evaluated, the Langmuir isotherm demonstrated the best fit, indicating that bacterial adsorption on the MAN-GO surface occurs as a uniform monolayer. The high R^2 value and close agreement between experimental and theoretical adsorption capacities confirm the Langmuir model's suitability for describing the adsorption behavior. The Q_{max}, representing the maximum adsorption capacity and reflecting the total bacterial load that the adsorbent can hold per unit mass, was determined to be 448.219 CFU g^{-1}, showcasing the adsorbent's high efficiency. Additionally, the R_L value of 4.638×10^{-9}, being near zero, signifies strong interactions between the adsorbent and adsorbate. The Langmuir constant, K_L, which relates to the adsorption energy, was found to be 2.973, indicating strong binding affinity and an efficient adsorption system.

Table 2 Computed parameters for various kinetic models and their corresponding correlation coefficients

Pseudo-first order		Pseudo-second order	
Parameters	Value	Parameters	Value
Q_e (calculated)	2.2529×10^7	Q_e (calculated)	2.032×10^7
Q_e (experimental)	1.987×10^7	Q_e (experimental)	1.987×10^7
K_1	8.337×10^{-3}	K_2	4.849×10^{-3}
R^2	0.917	R^2	0.999
Elovich model		**Intraparticle diffusion model**	
Parameters	Value	Parameters	Value
α	2.735×10^{-7}	K_{pi}	0.3801
β	3.655×10^6	C	2.004×10^6
R^2	0.943	R^2	0.995

3.8 Adsorption kinetics, analysis, and model fitting

The adsorption mechanism for *E. coli* was examined through adsorption kinetics, which offers critical evidence for the rate

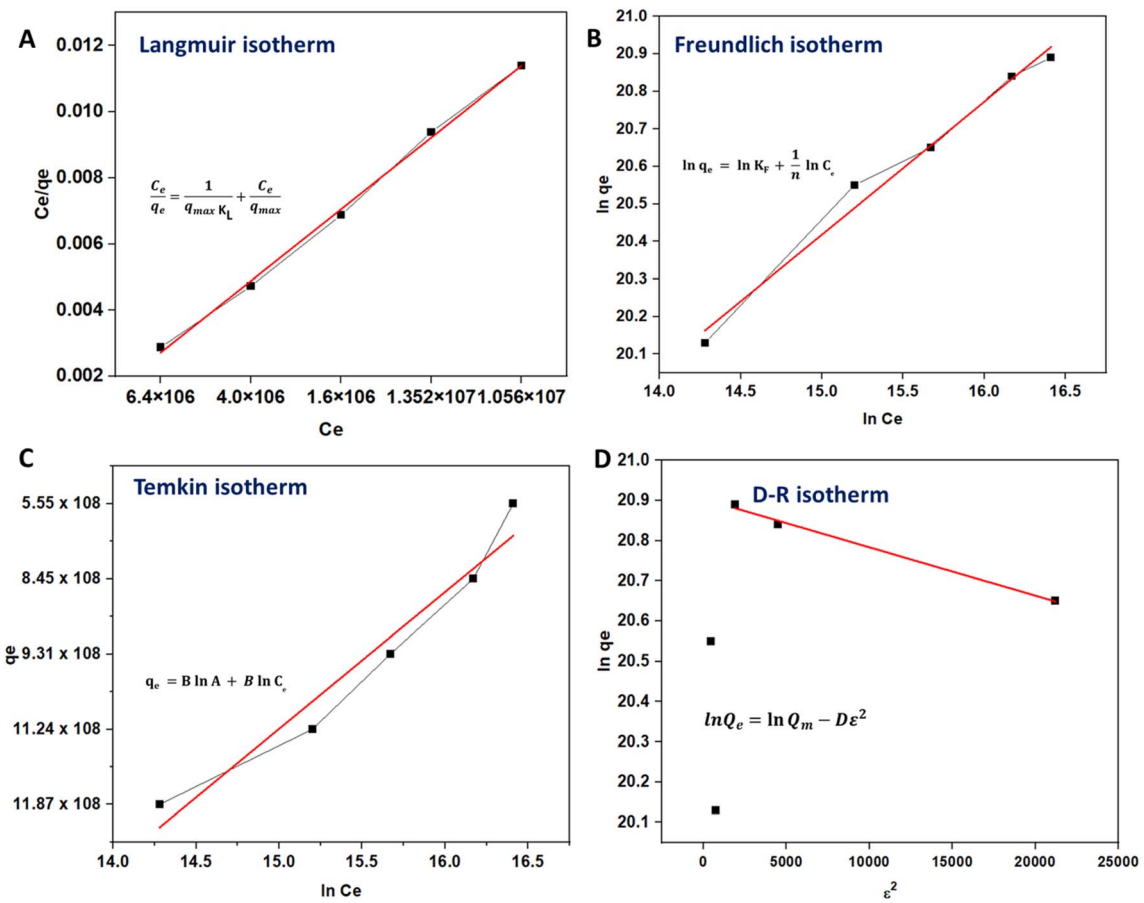

Fig. 15 Illustration and fitting of adsorption isotherm models for the studied system: (A) Langmuir isotherm, (B) Freundlich isotherm, (C) Temkin isotherm, and (D) Dubinin–Radushkevich (D–R) isotherm.

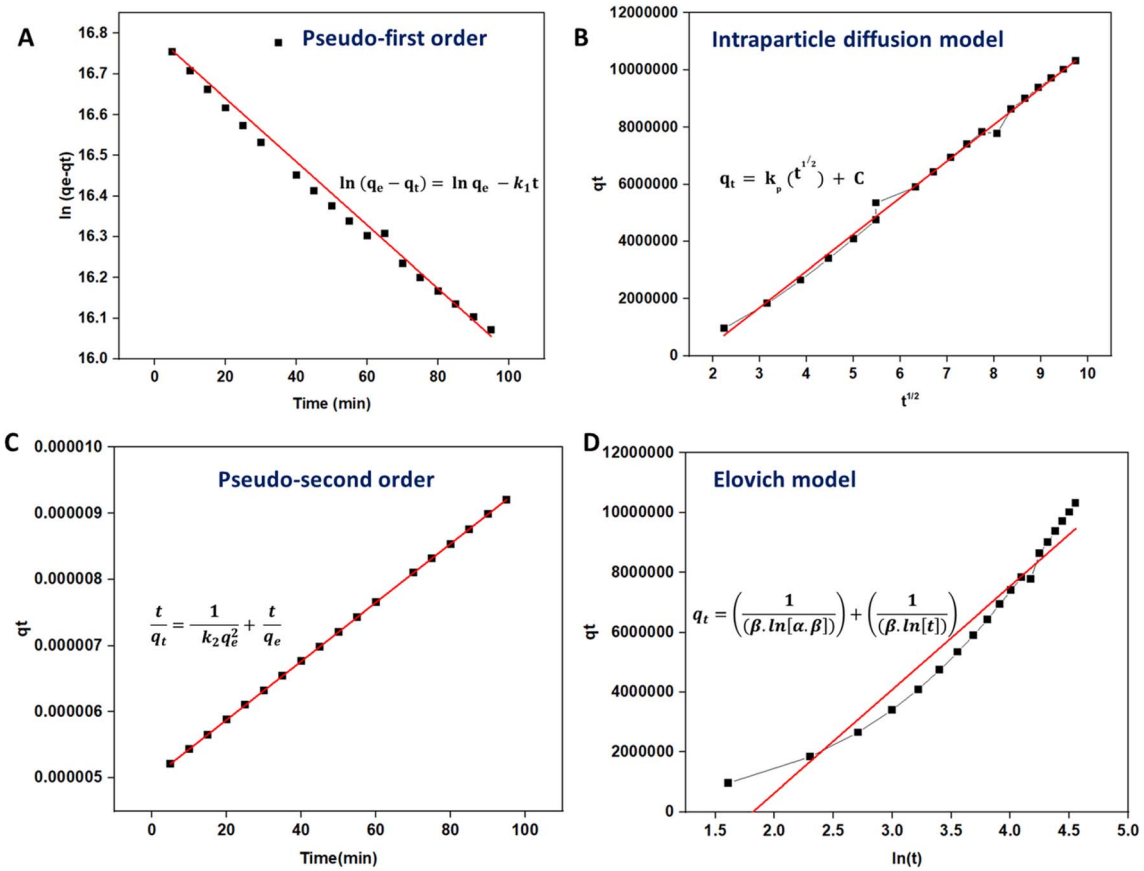

Fig. 16 Adsorption kinetic model fitting of the experimental data: (A) pseudo-first-order model, (B) pseudo-second-order model, (C) Elovich model, and (D) intraparticle diffusion model.

and efficiency of the adsorption process. Experimental studies on contact time demonstrated that the adsorbent effectively removed *E. coli*, with the adsorption equilibrium reached within a relatively short period. Kinetic models are vital for predicting adsorption behaviour, optimizing system design, and identifying the underlying mechanisms governing the process.[54,55]

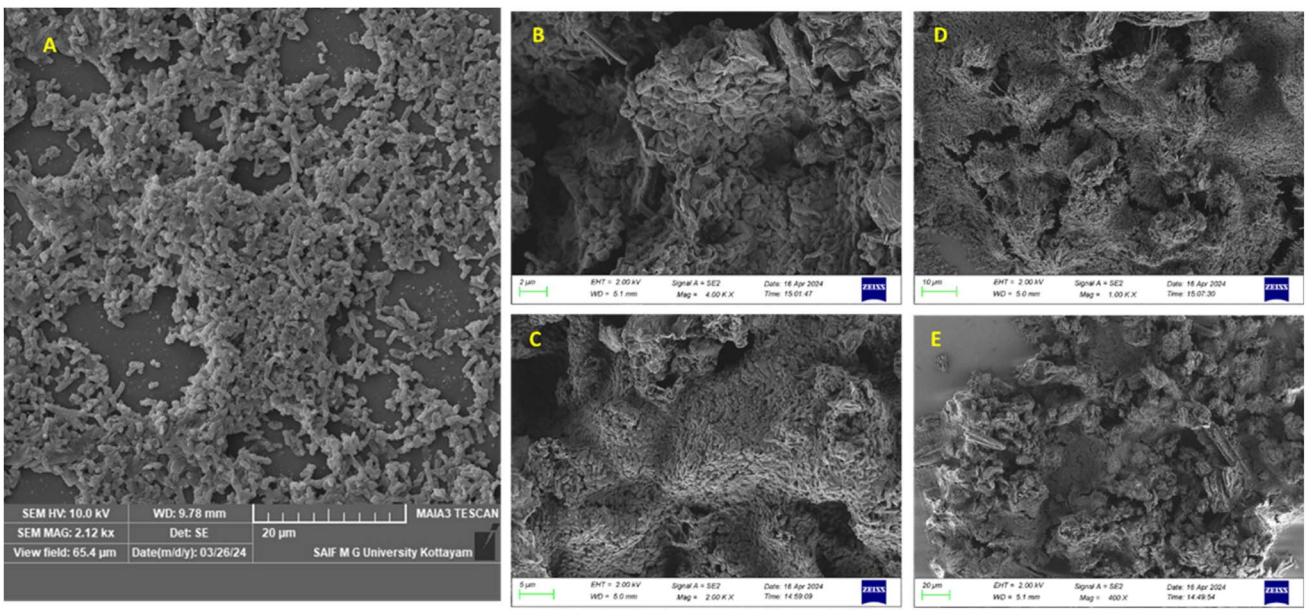

Fig. 17 SEM images illustrating *E. coli* bacteria and their interaction with mannosylated graphene oxide (MAN-GO). (A) SEM image of pristine *E. coli* bacteria. (B)–(E) SEM images showing *E. coli* bacteria adsorbed onto the MAN-GO surface.

The rapid adsorption has been attributed to the unique properties of MAN-GO, including its high surface area, abundant functional groups, and strong affinity for bacterial cells due to mannose-mediated interactions. These characteristics make it an efficient adsorbent for *E. coli* removal and enhance its potential for practical applications.

The adsorption kinetics were analysed, validated, and fitted to different models like pseudo-first order, pseudo-second order, Elovich and intraparticle diffusion models, among which the pseudo-second-order model demonstrated the best fit for the experimental data (Fig. 14A to D). The pseudo-second-order kinetic model is highly significant in adsorption studies as it provides detailed insights into the adsorption mechanism and the efficiency of the process.

The fitted parameters are tabulated in Table 2. A close agreement between Q_e (calculated) and Qe (experimental) confirms the model's reliability in describing the adsorption process. The K_2 rate constant is crucial for understanding the speed of adsorption and the interaction strength between the adsorbate and adsorbent.[56] The R^2 value, a measure of the model's goodness of fit, is critical for evaluating how well the kinetic model explains the experimental data; an R^2 value close to 1 demonstrates an excellent correlation and supports the use of the pseudo-second-order model for describing the adsorption behavior.

3.9 SEM analysis and BET surface area analysis of *E. coli* adsorption and desorption

Fig. 15 provides the morphological images of *E. coli* and its interaction with the MAN-GO composite. Fig. 15A illustrates the rod-shaped morphology of pure *E. coli*, characterized by smooth and well-defined cell walls. Fig. 15B–D depict *E. coli* adsorbed onto the MAN-GO composite at different magnifications. Upon adsorption onto MAN-GO, the bacteria are observed to attach firmly to the composite surface, often exhibiting slight morphological changes. The mannose coated GO sheets appear partially covered with bacterial cells, indicating strong interactions and effective adsorption. These results confirm the successful integration of *E. coli* with the material, showcasing the composite's potential for bacterial capture and sensing applications. The detailed elemental composition from EDS

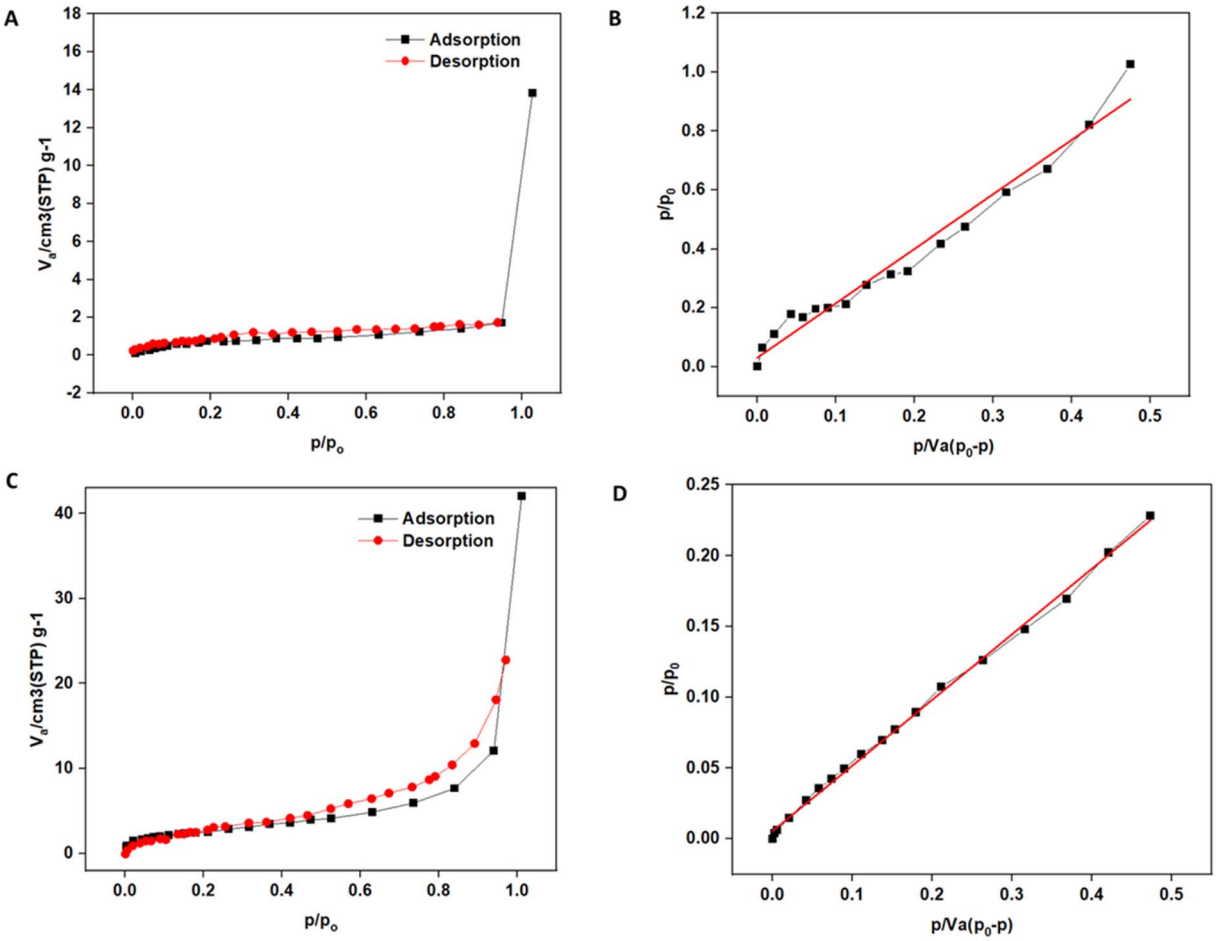

Fig. 18 Surface area and porosity analysis of mannosylated graphene oxide (MAN-GO) before and after *E. coli* adsorption. (A) Nitrogen adsorption–desorption isotherms of *E. coli*-adsorbed MAN-GO, (B) BET surface area plot of *E. coli*-adsorbed MAN-GO, (C) nitrogen adsorption–desorption isotherms of *E. coli*-desorbed MAN-GO, and (D) BET surface area plot of *E. coli*-desorbed MAN-GO.

mapping is given in Fig. S1 and S2 and Tables S1 and S2. BET analysis was conducted on *E. coli* adsorbed and desorbed MAN-GO using the BELSORP high-precision gas/vapor adsorption apparatus, following the same procedure outlined earlier (Fig. 16). Prior to analysis, the samples were degassed at 120 °C under vacuum for 3 hours to eliminate adsorbed moisture and impurities. Nitrogen adsorption–desorption isotherms were obtained at 77 K across a range of relative pressures. The detailed parameters, including surface area, pore size, and adsorption constants, are given in Tables S5 and S6. The BET analysis reveals significant differences between the adsorbed and desorbed states of the MAN-GO composite. The desorbed sample exhibits a substantially higher surface area of 9.721 m^2 g^{-1} and a pore volume of 0.051 cm^3 g^{-1} compared to the adsorbed sample values of 2.469 m^2 g^{-1} and 0.012 cm^3 g^{-1}, respectively, indicating that *E. coli* adsorption blocks active sites and occupies pores. Interestingly, the *E. coli*-adsorbed MAN-GO sample shows a higher surface area than pure MAN-GO, which may be attributed to the formation of a rough bacterial layer or structural rearrangements that expose additional surface regions. The monolayer adsorption capacity (Vm) also increases from 0.567 cm^3(STP)g^{-1} in the adsorbed state to 2.233 cm^3(STP) g^{-1} in the desorbed state, while the *C* constant of 81.423 for the adsorbed state highlights stronger adsorbate–surface interactions. Notably, the mean pore diameter remains nearly unchanged at 20 nm, indicating that the intrinsic pore structure of the material is preserved. These results confirm that *E. coli* adsorption reduces accessible surface properties, which are fully restored upon desorption, showcasing the composite's adsorption capacity and potential for reusability.

4 Mechansim of interaction of *E. coli* with D-mannose

The interaction mechanism of *E. coli* with MAN-GO involves both targeted binding and physical disruption of the bacterial cell membrane. Mannose functional groups on MAN-GO specifically bind to mannose-binding lectins (MBLs) on the *E. coli* surface, facilitating strong and selective adhesion.[57] Simultaneously, the sharp edges of graphene oxide sheets physically interact with the lipid bilayer of the bacterial membrane, causing disruptions and potential damage to the cell structure (Fig. 17).This cutting effect destabilizes the bacterial membrane, leading to leakage of intracellular components and further weakening the cells. In addition to the mechanical disruption, the wrapping effect of GO can ensure that the bacteria become isolated from their environment. The high surface area of graphene oxide allows for extensive contact with the bacterial surface, enhancing adsorption and interaction. These combined mechanisms—targeted mannose binding, physical cutting of the lipid layer, and efficient bacterial wrapping—ensure superior adsorption performance.[58,59] The synergy of chemical affinity and mechanical disruption highlights MAN-GO's effectiveness as a multifunctional material for bacterial removal and control. A schematic representation of the interaction of *E. coli* with MAN-GO is shown in Fig. 17.

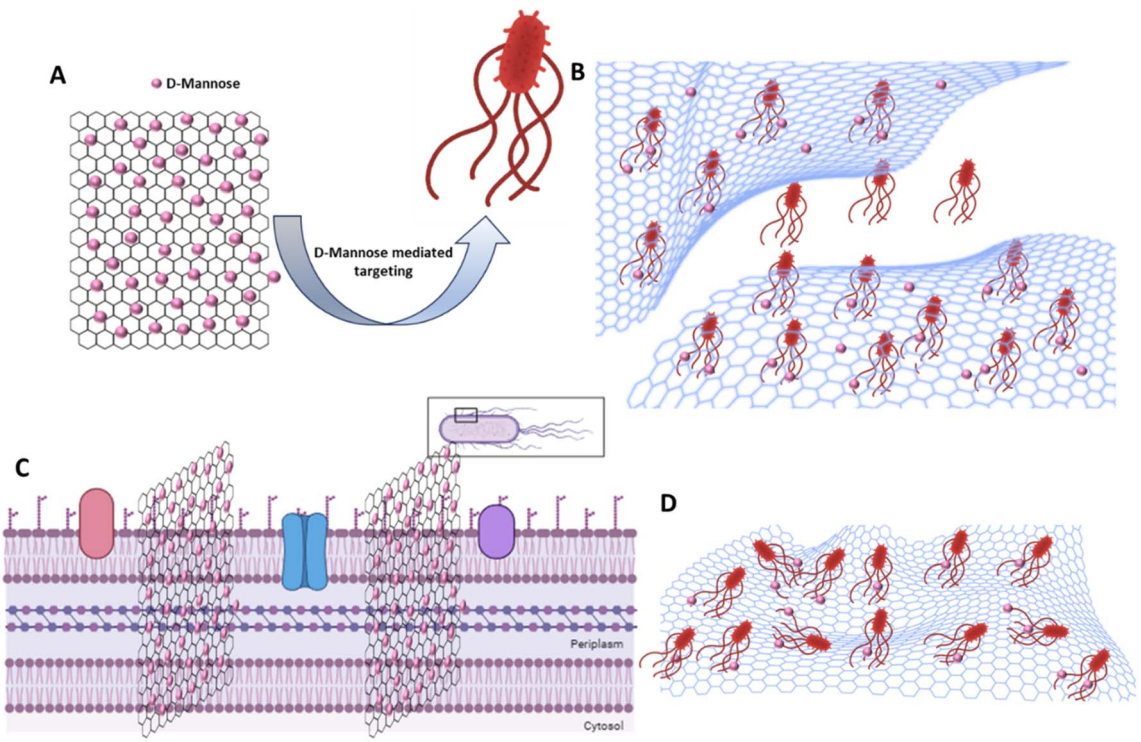

Fig. 19 (A) Schematic representation of *E. coli* interaction with MAN-GO, (B) mannose-facilitated wrapping of *E. coli*, (C) disruption of the lipid bilayer, and (D) adsorption of *E. coli* onto MAN-GO. Created with Biorender.com.

5 Conclusion

In summary, this study demonstrates the potential of a new composite system MAN-GO as a multifunctional material for the rapid and sensitive detection and effective removal of *E. coli* in diverse water systems. The composite's ability to achieve a low limit of detection (LOD) of 1.382×10^4 CFU mL^{-1} in fluorimetric assays underscores its high sensitivity and selectivity, even in complex matrices, while its demonstrated stability over four effective reuse cycles further highlights its practical applicability. The adsorption studies further validate the efficacy of MAN-GO, offering a maximum adsorption capacity of 448.219 CFU g^{-1}, rapid equilibrium within 120 minutes, and an adsorption efficiency of 88.21%. The system adheres to the pseudo-second-order kinetic model and Langmuir adsorption isotherm, confirming the strong and specific interaction between *E. coli* and the mannose-functionalized graphene oxide (Fig. 18).

The observed dual-functional capability positions MAN-GO as a promising material for real-world applications in microbial monitoring and water decontamination. Its "green" and sustainable approach eliminates the need for additional chemical agents, providing a cost-effective and environment-friendly solution to mitigate microbial contamination. Future work will focus on scaling up the system and exploring its performance in other environmental and clinical settings for practical implementation (Fig. 19).

Author contributions

Archana P K: conceptualization, reviewing and writing – original draft. Suni Vasudevan: conceptualization and supervision. Vidhya C. Valsalakumar: conceptualization. Unnikrishnan Gopalakrishna Panicker: editing and validation. All authors have given approval to the final version of the manuscript.

Conflicts of interest

The authors declare no competing financial interest.

Data availability

The data supporting this article have been included as part of the supplementary information (SI). Supplementary information: EDS spectra and elemental composition of *E. coli* (Fig. S1, Table S1) and *E. coli* adsorbed on MAN-GO (Fig. S2, Table S2); BET analysis parameters of MAN-GO, GO, and their *E. coli* adsorbed counterparts (Tables S3–S6); composition details of fluorescence interference study groups (Table S7); UV-visible absorption spectra of GO, MAN-GO, and *E. coli* control (Fig. S3); and performance evaluation of the sensor system for *E. coli* detection (Fig. S4). See DOI: https://doi.org/10.1039/d5na00948k.

Acknowledgements

Archana P. K., gratefully acknowledges financial support from the Ministry of Human Resource Development, Govt. of India, in the form of a GATE Fellowship. We would like to express our gratitude to Aswini Diagnostics, Calicut, for providing *E. coli* strains essential for this research. Their support was invaluable in facilitating the experimental work presented in this study. We extend our sincere gratitude to Ms. Anjali for her assistance with bacterial culture and to Prof. A. Sujith for providing the necessary facilities for this research. The authors would like to thank NIT Calicut for providing all the necessary resources for the research.

References

1 B. Pérez-López and A. Merkoçi, *Trends Food Sci. Technol.*, 2011, **22**, 625–639.
2 S. Mao, J. Chang, G. Zhou and J. Chen, *Small*, 2015, **11**, 5336–5359.
3 S. Yao, P. Swetha and Y. Zhu, *Adv. Healthc. Mater.*, 2018, **7**, 1700889.
4 S. Malik, J. Singh, R. Goyat, Y. Saharan, V. Chaudhry, A. Umar, A. A. Ibrahim, S. Akbar, S. Ameen and S. Baskoutas, *Heliyon*, 2023, **9**, e19929.
5 K. Xu, C. Fu, Z. Gao, F. Wei, Y. Ying, C. Xu and G. Fu, *Instrum. Sci. Technol.*, 2018, **46**, 115–145.
6 X. Sui, J. R. Downing, M. C. Hersam and J. Chen, *Mater. Today*, 2021, **48**, 135–154.
7 K. Singh, R. Jaiswal, R. Kumar, S. Singh and K. Agarwal, *Bull. Mater. Sci.*, 2023, **46**, 79.
8 K. Wise and M. Brasuel, *Nanotechnol. Sci. Appl.*, 2011, **4**, 73–86.
9 S. Su, W. Wu, J. Gao, J. Lu and C. Fan, *J. Mater. Chem.*, 2012, **22**, 18101–18110.
10 L. Rose, X. A. Mary, I. Johnson, G. Srinivasan, L. Priya and J. Bhagavathsingh, *Sci. Rep.*, 2021, **11**, 1–11.
11 H. Huang, S. Su, N. Wu, H. Wan, S. Wan, H. Bi and L. Sun, *Front. Chem.*, 2019, **7**, 1–26.
12 S. K. Metkar and K. Girigoswami, *Biocatal. Agric. Biotechnol.*, 2019, **17**, 271–283.
13 S. Panda, S. Hajra, H. G. Kim, H. Jeong, P. G. R. Achary, S. Hong, B. Dudem, S. R. P. Silva, V. Vivekananthan and H. J. Kim, *J. Mater. Chem. B*, 2023, **11**, 10147–10157.
14 Y. Yao, G. Xie, X. Zhang, J. Yuan, Y. Hou and H. Chen, *Anal. Methods*, 2021, **13**, 2209–2214.
15 T. Li, F. Zhu, W. Guo, H. Gu, J. Zhao, M. Yan and S. Liu, *RSC Adv.*, 2017, **7**, 30446–30452.
16 T. Sanji, K. Shiraishi, M. Nakamura and M. Tanaka, *Chem. - An Asian J.*, 2010, **5**, 817–824.
17 S. Nair, V. Kumar, R. Kumar, V. K. Jain and S. Nagpal, *Int. J. Mater. Res.*, 2022, **113**, 560–568.
18 J. Carrillo-Gómez, C. Durán-Acevedo and R. García-Rico, *Water*, 2019, **11**, 1–15.
19 B. Thakur, G. Zhou, J. Chang, H. Pu, B. Jin, X. Sui, X. Yuan, C. H. Yang, M. Magruder and J. Chen, *Biosens. Bioelectron.*, 2018, **110**, 16–22.

20 S. Hazir, H. K. Kaya, M. Touray, H. Çimen and D. Shapiro-Ilan, *Turkish J. Zool.*, 2022, **46**, 305–350.
21 H. Xu, F. Tang, J. Dai, C. Wang and X. Zhou, *BMC Microbiol.*, 2018, **18**, 1–6.
22 Z. Li, Y. Jiang, S. Tang, H. Zou, W. Wang, G. Qi, H. Zhang, K. Jin, Y. Wang, H. Chen, L. Zhang and X. Qu, *Microchim. Acta*, 2024, **13**, 20240056.
23 Z. Sun, S. Wu, Y. Peng, M. Wang, M. Jalalah, M. S. Al-Assiri, F. A. Harraz, J. Yang and G. Li, *Chem. Eng. J.*, 2021, **405**, 126707.
24 J. K. Ajish, K. S. Ajish Kumar, A. Ruhela, M. Subramanian, A. D. Ballal and M. Kumar, *Sensors Actuators, B Chem.*, 2018, **255**, 1726–1734.
25 V. C. Valsalakumar, A. S. Joseph, J. Piyus and S. Vasudevan, *ACS Appl. Nano Mater.*, 2023, **6**, 8382–8395.
26 S. Suguna, C. I. David, J. Prabhu and R. Nandhakumar, *Mater. Adv.*, 2021, **2**, 6197–6212.
27 V. Georgakilas, M. Otyepka, A. B. Bourlinos, V. Chandra, N. Kim, K. C. Kemp, P. Hobza, R. Zboril and K. S. Kim,.
28 A. M. El-Khawaga, H. Tantawy, M. A. Elsayed and A. I. A. Abd El-Mageed, *Sci. Rep.*, 2022, **12**, 1–13.
29 O. H. Abuzeyad, A. M. El-Khawaga, H. Tantawy, M. Gobara and M. A. Elsayed, *Discov. Nano*, 2025, **20**, 2.
30 O. H. Abuzeyad, A. M. El-Khawaga, H. Tantawy and M. A. Elsayed, *J. Mol. Struct.*, 2023, **1288**, 135787.
31 W. S. Hummers and R. E. Offeman, *J. Am. Chem. Soc.*, 1958, **80**, 1339.
32 N. I. Zaaba, K. L. Foo, U. Hashim, S. J. Tan, W. W. Liu and C. H. Voon, *Procedia Eng.*, 2017, **184**, 469–477.
33 M. de Sousa, D. S. T. Martinez and O. L. Alves, *J. Nanoparticle Res.*, 2022, **27**, 21.
34 M. De Sousa, C. H. Z. Martins, L. S. Franqui, L. C. Fonseca, F. S. Delite, E. M. Lanzoni, D. S. T. Martinez and O. L. Alves, *J. Mater. Chem. B*, 2018, **6**, 2803–2812.
35 U. A. Kanta, V. Thongpool, W. Sangkhun, N. Wongyao and J. Wootthikanokkhan, *J. Nanomater.*, 2017, **13**, 2758294.
36 S. R. B. Nazri, W. W. Liu, C. S. Khe, N. M. S. Hidayah, Y. P. Teoh, C. H. Voon, H. C. Lee and P. Y. P. Adelyn, *AIP Conf. Proc.*, 2018, **2045**, 020033.
37 B. Khodadadi Chegeni, A. Dadkhah Tehrani and M. Adeli, *J. Taiwan Inst. Chem. Eng.*, 2019, **96**, 176–184.
38 B. Massoumi, F. Ghandomi, M. Abbasian, M. Eskandani and M. Jaymand, *Appl. Phys. A Mater. Sci. Process.*, 2016, **122**, 1–13.
39 K. Haubner, J. Murawski, P. Olk, L. M. Eng, C. Ziegler, B. Adolphi and E. Jaehne, *ChemPhysChem*, 2010, **11**, 2131–2139.
40 L. Z. Guan, Y. J. Wan, L. X. Gong, D. Yan, L. C. Tang, L. Bin Wu, J. X. Jiang and G. Q. Lai, *J. Mater. Chem. A*, 2014, **2**, 15058–15069.
41 C. A. Tao, J. Wang, S. Qin, Y. Lv, Y. Long, H. Zhu and Z. Jiang, *J. Mater. Chem.*, 2012, **22**, 24856–24861.
42 S. Drewniak, R. Muzyka, A. Stolarczyk, T. Pustelny, M. Kotyczka-Morańska and M. Setkiewicz, *Sensors*, 2016, **16**, 103.
43 J. Shang, L. Ma, J. Li, W. Ai, T. Yu and G. G. Gurzadyan, *Sci. Rep.*, 2012, **2**, 1–8.
44 S. Zafar, S. Krishna Mani, M. Monisha and B. Lochab, *RSC Sustain.*, 2024, **3**, 365–375.
45 W. Zi, K. Jurkiewicz, A. Burian, M. Pawlyta, S. Boncel, J. Kubacki, P. Kowalczyk, K. Krukiewicz, A. Furuse, K. Kaneko and A. P. Terzyk, *ACS Appl. Nano Mater.*, 2022, **5**, 18448–18461.
46 B. G. Ghule, N. M. Shinde, S. D. Raut, S. F. Shaikh, A. M. Al-Enizi, K. H. Kim and R. S. Mane, *J. Colloid Interface Sci.*, 2021, **589**, 401–410.
47 T. H. Han, Y. K. Huang, A. T. L. Tan, V. P. Dravid and J. Huang, *J. Am. Chem. Soc.*, 2011, **133**, 15264–15267.
48 C. Su, M. Acik, K. Takai, J. Lu, S. J. Hao, Y. Zheng, P. Wu, Q. Bao, T. Enoki, Y. J. Chabal and K. P. Loh, *Nat. Commun.*, 2012, **3**, 1298–1299.
49 Y. Deng, J. H. Ryu and L. R. Beuchat, *Int. J. Food Microbiol.*, 1998, **45**, 173–184.
50 P. Kumar and A. Libchaber, *Biophys. J.*, 2013, **105**, 783–793.
51 S. M. Saad, J. Abdullah, S. Abd Rashid, Y. W. Fen, F. Salam and L. H. Yih, *Meas. J. Int. Meas. Confed.*, 2020, **160**, 107845.
52 S. N. Aisyiyah Jenie, Y. Kusumastuti, F. S. H. Krismastuti, Y. M. Untoro, R. T. Dewi, L. Z. Udin and N. Artanti, *Sensors*, 2021, **21**, 1–13.
53 J. P. Maity, C. M. Hsu, T. J. Lin, W. C. Lee, P. Bhattacharya, J. Bundschuh and C. Y. Chen, *Environ. Nanotechnology, Monit. Manag.*, 2018, **9**, 18–28.
54 Z. Raji, A. Karim, A. Karam and S. Khalloufi, *Waste*, 2023, **1**, 775–805.
55 M. A. Al-Ghouti, M. Y. Ashfaq, M. Khan, Z. Al Disi, D. A. Da'na and R. Shoshaa, *Sci. Total Environ.*, 2023, **895**, 164854.
56 V. C. Valsalakumar, Y. Sreevalli, A. P. K, A. S. Joseph, S. Ubaid and S. Vasudevan, *J. Environ. Manage.*, 2024, **368**, 122068.
57 J. Ramos-Soriano, M. Ghirardello and M. C. Galan, *Chem. Soc. Rev.*, 2022, **51**, 9960–9985.
58 C. Sharma, A. K. Shukla, M. Verma, M. Bathla and A. Acharya, *Environ. Sci. Nano*, 2023, **10**, 1077–1095.
59 G. G. Montes-Duarte, G. Tostado-Blázquez, K. L. S. Castro, J. R. Araujo, C. A. Achete, J. L. Sánchez-Salas and J. Campos-Delgado, *RSC Adv.*, 2021, **11**, 6509–6516.

